



# TROPOMI-Retrieved Underwater Light Attenuation in Three Spectral Regions in the Ultraviolet and Blue

Julia Oelker<sup>1,2</sup>, Svetlana N. Losa<sup>2,3</sup>, Andreas Richter<sup>1</sup> and Astrid Bracher<sup>1,2\*</sup>

<sup>1</sup> Department of Physics and Electrical Engineering, Institute of Environmental Physics, University of Bremen, Bremen, Germany, <sup>2</sup> Phytooptics Group, Physical Oceanography of Polar Seas, Climate Sciences, Alfred Wegener Institute, Helmholtz Centre for Polar and Marine Research, Bremerhaven, Germany, <sup>3</sup> Shirshov Institute of Oceanology, Russian Academy of Sciences, Moscow, Russia

## OPEN ACCESS

### Edited by:

Griet Neukermans,  
Ghent University, Belgium

### Reviewed by:

Zhongping Lee,  
University of Massachusetts Boston,  
United States

Jian Xu,  
National Space Science Center (CAS),  
China

Cédric Jamet,  
UMR8187 Laboratoire d'océanologie  
et de Géosciences (LOG), France

### \*Correspondence:

Astrid Bracher  
astrid.bracher@awi.de

### Specialty section:

This article was submitted to  
Ocean Observation,  
a section of the journal  
Frontiers in Marine Science

**Received:** 01 October 2021

**Accepted:** 14 February 2022

**Published:** 17 March 2022

### Citation:

Oelker J, Losa SN, Richter A and  
Bracher A (2022) TROPOMI-Retrieved  
Underwater Light Attenuation in Three  
Spectral Regions in the Ultraviolet and  
Blue. *Front. Mar. Sci.* 9:787992.  
doi: 10.3389/fmars.2022.787992

Ultraviolet (UV) radiation plays an important role in the ocean for the biogeochemical cycling through photooxidation of colored dissolved organic matter and metals. It also influences the release of trace gases into the atmosphere. Understanding interaction and climate feedback mechanisms of these processes requires global long-term monitoring of UV radiation in the ocean. Ocean color sensors provide the diffuse attenuation coefficient for downwelling solar irradiance ( $K_d$ ) as an estimate for the mean light penetration depth in the surface ocean. However,  $K_d$  products for the UV spectral range are currently only indirectly inferred from measurements in the visible spectral region. We exploit the UV and visible wavelengths of the TROPOMI sensor onboard Sentinel-5P to directly infer diffuse attenuation coefficients in the UV and blue spectral range. Our approach is based on Differential Optical Absorption Spectroscopy in combination with radiative transfer modeling which has been used in earlier studies to successfully derive  $K_d$  in the blue from the vibrational Raman scattering (VRS) signal. VRS was detected in the backscattered radiances of TROPOMI-like sensors at a spectral resolution around 0.5 nm. We adapt this method for the TROPOMI sensor and more spectral regions to obtain two novel  $K_d$  products in the UV range (312.5–338.5 nm and 356.5–390 nm), additionally to the blue  $K_d$  (390–423 nm). One month of TROPOMI data show high sensitivity to retrieve VRS (fit errors <15%). The resulting  $K_d$  values in the UV and blue agree reasonably (RMSD <0.31 m<sup>-1</sup>) with *in-situ* data measured during a transatlantic cruise.  $K_d$ -blue compared to wavelength-converted  $K_d(490)$  products from OLCI and OC-CCI shows that the differences between the three data sets are within uncertainties given for the OC-CCI product. TROPOMI  $K_d$ -blue results have higher quality and much higher spatial coverage and resolution than previous ones from SCIAMACHY, GOME-2, and OMI. Perspectively, global TROPOMI  $K_d$  products, once thoroughly validated, can be used as input for modeling, e.g., photochemical reaction rates of climatically important compounds and inhibition of primary productivity.

**Keywords:** diffuse attenuation coefficient, ultraviolet radiation, TROPOMI, DOAS, ocean color

## 1. INTRODUCTION

Light governs large-scale biological, physical, and chemical processes in the ocean. Incoming radiation heats the ocean thereby influencing mixed layer dynamics (Ohlmann et al., 1996) and ocean circulation, which in turn is coupled to atmospheric temperature and circulation (Lewis et al., 1990; Miller et al., 2003; Shell et al., 2003). Optically active biological and chemical constituents influence the heat and radiation budget of the ocean (Sathyendranath et al., 1991; Morel and Antoine, 1994; Frouin and Iacobellis, 2002). Visible radiation controls primary productivity of phytoplankton and higher aquatic plants (Sathyendranath et al., 1989) and thus the base of almost all life in the ocean. In contrast, ultraviolet (UV) radiation damages phytoplankton cells and other microorganisms (Cullen and Neale, 1994; Sinha and Hader, 2002). Interactions between climate change and UV radiation penetrating the ocean and its effect on biogeochemical cycles are complex (Zepp et al., 2003, 2007). Upon photodegradation of colored dissolved organic matter (CDOM), the primary absorber of UV radiation in the ocean (Siegel et al., 2002), light penetration and nutrient availability increase. UV radiation also affects bioavailability of iron, copper, and other trace metals and the exchange of trace gases across the air-sea interface, changing atmospheric chemistry.

Adequately describing these light-ocean interaction processes and their role in biogeochemical cycling and climate change feedback mechanisms requires measurements of radiation parameters on a regular basis and large scales (IOCCG, 2008). Ocean color satellite missions routinely monitor the global ocean from space providing some insight into radiation in the ocean (Frouin et al., 2018). Standard products that are operationally provided are the photosynthetically available radiation above the surface (PAR) and the diffuse attenuation coefficient ( $K_d$ ) at 490 nm ( $K_d(490)$ ).  $K_d$  describes how fast the incoming light diminishes with depth. The mean  $K_d$  over distant depths  $z_1$  and  $z_2$  can be calculated from the plane downwelling irradiance  $E_d$  as (Lee et al., 2005b).

$$K_d(z_1 \leftrightarrow z_2, \lambda) = \frac{1}{z_2 - z_1} \ln \left( \frac{E_d(z_1, \lambda)}{E_d(z_2, \lambda)} \right) \quad (1)$$

with wavelength  $\lambda$ . From passive remote sensing, the average  $K_d$  of the surface ocean can be retrieved. It contains information on the first optical depth, i.e., the depth at which the plane downwelling irradiance below the ocean surface has decreased to around 37%. It is a valuable parameter used for estimating, e.g., heat budget (Lewis et al., 1990; Morel and Antoine, 1994; Kara et al., 2004) and primary productivity (Platt, 1986; Sathyendranath et al., 1989).  $K_d(490)$  and  $K_d$  at other wavelengths ( $K_d(\lambda)$ ) can be calculated from ocean color satellite data using empirical (based on band ratios, e.g., Austin and Petzold, 1981; Morel and Maritorena, 2001; Shen et al., 2017), semi-analytical (Lee et al., 2005b; Morel et al., 2007b; Wang et al., 2009), or neural network (Jamet et al., 2012) approaches.

Current ocean color satellites provide only limited information on light reflected from the ocean in the UV.

For most ocean color sensors, the shortest wavelength band lies around 412 nm, some reach down to 380 nm (e.g., Second-Generation Global Imager on GCOM-C, Okamura et al., 2019). The only recent OC sensor with a band at shorter wavelengths, 355 nm, is the Ultraviolet Imager on HaiYang-1C satellite launched in 2018 (<http://www.nsoas.org.cn/eng/item/204.html>). Future missions also aim at providing measurements in the UV spectral range. For instance, the Ocean Color Instrument of the upcoming PACE mission is planned to record radiances from 340 nm with spectral resolution of 5 nm. However, the PACE mission will not be launched before November 2023 (<https://pace.oceansciences.org/>). So far, the only existing UV product for ocean color applications is the above-surface planar spectral UV irradiance at noon from the hyperspectral Ozone Monitoring Instrument (OMI) (Tanskanen et al., 2006). Information on  $K_d$  in the UV has been indirectly obtained from ocean color information at visible wavelengths in several studies.  $K_d$  in the UV is empirically related to  $K_d$  or absorption at visible wavebands (Smyth, 2011; Lee et al., 2013), blue-green reflectance ratios (Johannessen et al., 2003), or principle components of visible reflectances remote-sensing reflectance ( $R_{rs}$ ) (Fichot et al., 2008) or it is estimated using an ocean case-I UV model with the chlorophyll-a concentration (Chla) from ocean color sensors as input (Vasilkov et al., 2005). All of these approaches rely on the rather weak relationship of optical properties between the UV and visible wavelength range (Vasilkov et al., 2002a; Morel et al., 2007a). Wang et al. (2021) developed a deep-learning system to obtain  $R_{rs}$  in the UV from  $R_{rs}$  at visible bands; then  $R_{rs}(\text{UV})$  was used to derive  $K_d$  at 360, 380, and 400 nm. They demonstrate the non-linearity between  $R_{rs}$  at UV and visible wavelengths. Frouin et al. (2018) have summarized user needs for radiometric satellite products, revealing a need for information on ocean radiation in the UV. They suggest to fill parts of this knowledge gap by utilizing current satellite missions such as Sentinel-5P for UV products.

In this study, we exploit Sentinel-5P Tropospheric Monitoring Instrument's (TROPOMI) UV and visible bands for deriving two novel  $K_d$  products in the UV. These products describe the average  $K_d$  in the wavelength regions 312.5 to 338.5 nm and 356.5 to 390 nm for the first optical depth. In addition, we derive the average  $K_d$  in the range 390 to 423 nm. Our approach is based on earlier studies deriving this latter  $K_d$  in the blue spectral range from SCIAMACHY (Scanning Imaging Absorption Spectrometer for Atmospheric CHartography), GOME-2 (Global Ozone Monitoring Experiment 2), and OMI satellite data (Dinter et al., 2015; Oelker et al., 2019). Differential Optical Absorption Spectroscopy (DOAS) is used to target the Vibrational Raman Scattering (VRS) signal in the ocean. The number of these inelastic scattering processes depends on the number of photons in the ocean and causes filling-in of absorption structures such as Fraunhofer lines in the solar spectrum. Because VRS is negligible in the atmosphere, the VRS signal found in backscattered radiances measured by satellites can be linked to the radiation in the ocean using radiative transfer simulations.

Our study conceptually shows the feasibility by presenting first results of the novel  $K_d$ -UV products and the  $K_d$ -blue product.

We focus on 1 month of TROPOMI data in 2018, 11 May to 9 June, for which *in-situ*  $K_d(\lambda)$  data is available from a R/V Polarstern cruise transecting the Atlantic Ocean from Punta Arenas, Chile, to Bremerhaven, Germany. The quality of these  $K_d$  products is evaluated against this *in-situ* data set and wavelength-converted multispectral  $K_d$  products from the Ocean Colour Climate Change Initiative (OC-CCI) data set and the Sentinel-3A Ocean and Land Colour Instrument (OLCI).

## 2. MATERIALS AND METHODS

### 2.1. Data Sets

#### 2.1.1. TROPOMI Data

The satellite Sentinel-5 Precursor (S5P) hosts the Tropospheric Monitoring Instrument (TROPOMI) (Veefkind et al., 2012). It is in a low Earth orbit and its standard level 2 products provide daily global measurements of atmospheric trace gases and aerosols. The satellite was launched in October 2017. Local solar time at ascending node is 13:30. TROPOMI measures backscattered radiances at a spatial resolution of 3.5 by 7 km at nadir which was improved to 3.5 by 5.5 km in August 2019 due to high signal-to-noise performance. Once per day the solar irradiance is recorded. Measurements are taken in push-broom configuration at a swath width of 2,600 km providing daily global coverage. TROPOMI has spectral bands in the UV, visible (VIS), near-infrared, and the shortwave infrared. Relevant for developing the  $K_d$  products in this study are band 3 (UV) from 310 to 405 nm and band 4 (VIS) from 405 to 500 nm. Spectral resolution of these bands is around 0.55 nm. We used level 1b TROPOMI radiances V01.00.00 and corresponding daily UVN (bands 1 to 6) irradiances (Vonk, 2018). Clouds shield the radiance signal from the ocean, so the TROPOMI data set was filtered for cloud-free scenes using a cloud fraction of 0.05 as threshold. Cloud fractions were taken from FRESCO type cloud retrieval in the nitrogen dioxide fit window (van Geffen et al., 2019). Pixels over land and inland waters were removed from the data set.

#### 2.1.2. In-situ Data

Radiometric data was collected from 11 May to 9 June 2018 on Polarstern expedition PS113, crossing the Atlantic from Punta Arenas, Chile, to Bremerhaven, Germany. Two irradiance sensors (RAMSES ACC-2-VIS, TriOS GmbH, Germany) covering the wavelength region from 320 nm to 950 nm with a spectral sampling of 3.3 nm, resolution of 10 nm, and accuracy of 0.3 nm were used to measure the underwater downwelling irradiance  $E_d(z, \lambda)$ . One sensor was mounted to a steel frame for vertical profiling at 0.1 m/s down to 130 m at a distance of 5 m to the ship, outside of the ship's shading, at 19 discrete stations. It is additionally equipped with an inclination and pressure sensor. The second sensor was mounted on an undulating platform (Triaxus, extended version, MacArtney, Denmark) towed behind the research vessel at a speed of 8 knots for several transects along the cruise track. Vertical movement of the Triaxus was 1 m/s. The depth was determined with a Seabird CTD mounted to the Triaxus and the inclination in all directions was recorded by the Triaxus hardware. Measurements were taken with automatically adjusted integration times between 4 and 8 s. Triaxus profile

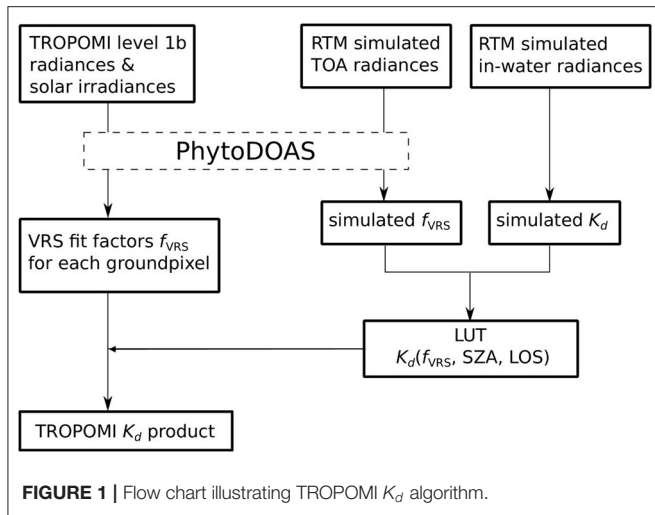
data was only processed if the euphotic depth was reached and values of the downwelling irradiance at 15 m depth and a wavelength of 400 nm were greater than  $150 \text{ mW m}^{-2} \text{ nm}^{-1}$  (all station data fulfilled these criteria). Radiometric data from 6 transects between 2 and 48 h long were identified useful for determining  $K_d(\lambda)$ . Generally, profile measurements were only valid if the instrument's inclination in either dimension was  $< 14^\circ$ . A third RAMSES ACC-2-VIS sensor mounted on top of the ship recorded the incident downwelling irradiance above the surface  $E_d(\lambda, 0^+)$ , to correct for incident sunlight variations. Mean  $K_d$  was calculated from  $E_d(z, \lambda)$  profiles mostly over the depth interval 7 to 22 m for the stations and 7 to 30 m, some 7 to 60 m, for the Triaxus profiles.  $K_d$ -UVAB,  $K_d$ -UVA and  $K_d$ -blue used for validation were derived as described in section 2.3.3 for the simulations. Details on measurement procedure can be found in Bracher et al. (2020). *In situ*  $K_d$  data are available at Bracher and Dinter (2021), Bracher et al. (2022).

### 2.2. Multispectral Satellite Data

Derived  $K_d$  products from TROPOMI were compared to  $K_d(490)$  from Sentinel-3A OLCI and the OC-CCI data set. OLCI onboard Sentinel-3A has a spatial resolution of 300 m. Ocean color information is obtained from 21 spectral bands. The operational  $K_d(490)$  product is calculated based on the OK2-560 algorithm (Morel et al., 2007b) which is based on an empirical relation between  $\text{Chla}$  and  $K_d(490)$ , with  $\text{Chla}$  derived from an empirical band-ratio algorithm. OLCI data was downloaded *via* EUMETSAT Streaming Service (version IPF 6.11, processing baseline v2.23). As second multispectral data set, the OC-CCI data set (Sathyendranath et al., 2019) version 4.2 (Sathyendranath et al., 2020) (<http://www.esa-oceancolour-cci.org>) was used. It is a merged product consisting of information from the MODIS-Aqua and VIIRS sensors for 2018. Data is provided on a sinusoidal grid with 4 km spatial and daily temporal resolution.  $K_d(490)$  is retrieved semi-analytically (Lee et al., 2005b). Absorption and backscattering are first obtained in a quasi-analytical approach (Lee et al., 2002) and then related to  $K_d(490)$  using look-up tables (LUTs) established with radiative transfer modeling.

### 2.3. Algorithm

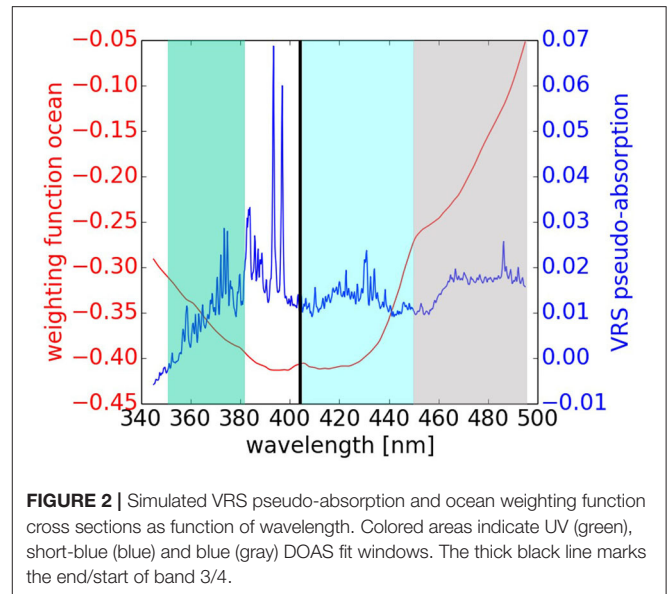
Vibrational Raman Scattering (VRS) is an inelastic scattering process which occurs in the ocean when photons scatter off water molecules (Walrafen, 1966). It therefore contains information of the number of photons in the ocean. Photons are scattered to longer wavelengths with a wavelength shift of 33 to 99 nm in the UV-VIS (Haltrin and Kattawar, 1993). Absorption features such as Fraunhofer lines in the solar spectrum filled-in by these photons are detectable in backscattered radiances recorded by satellites, appearing as a so-called pseudo-absorption, known as the Ring effect (Grainger and Ring, 1962). Using Differential Optical Absorption Spectroscopy (DOAS), the VRS signal can be identified in backscattered radiances from satellite sensors with sufficient spectral resolution ( $\sim 0.5 \text{ nm}$ ) (Vasilkov et al., 2002b; Vountas et al., 2003, 2007). Since VRS is negligible in the atmosphere (Vountas et al., 1998), Dinter et al. (2015) exploited



these spectral features to infer the light availability and  $K_d$  in the ocean from SCIAMACHY backscattered radiances via radiative transfer modeling. Oelker et al. (2019) closely followed this approach with some modifications on DOAS and RTM settings to derive  $K_d$  from SCIAMACHY and additionally OMI and GOME-2 for nearly 1 year of data in 2007. We based our algorithm on these earlier works with minor modifications and extended it to the UV spectral region. In the following, we summarize the retrieval steps for deriving  $K_d$  from VRS, see also the flowchart in **Figure 1**.

### 2.3.1. PhytoDOAS

Differential Optical Absorption Spectroscopy (DOAS) (Perner and Platt, 1979) is a method for inferring atmospheric trace gas concentrations from high-frequency absorption features in backscattered radiances. The optical depth  $\tau$  is calculated from backscattered radiances  $I$  divided by a reference spectrum, e.g., an extra-terrestrial solar spectrum  $I_0$ . Low-frequency features such as Rayleigh and aerosol scattering and aerosol absorption are removed by subtracting a low-order polynomial. Absorption spectra of atmospheric trace gases are fitted to the high-frequency part of the optical depth to infer their concentrations. DOAS has been extended to the ocean domain (PhytoDOAS) for retrieving phytoplankton functional types (Bracher et al., 2009; Sadeghi et al., 2012), light availability (Dinter et al., 2015),  $K_d$  (Dinter et al., 2015; Oelker et al., 2019) through VRS (Vountas et al., 2003, 2007), and phytoplankton fluorescence (Wolanin et al., 2015) by including (pseudo-) absorption spectra for oceanic constituents and inelastic processes. Inelastic scattering processes, such as VRS, lead to filling-in of Fraunhofer lines. These are treated as pseudo-absorbers in DOAS. Following the model established by Vountas et al. (1998) their compensation spectra (named pseudo-absorption cross section which is unit-less)  $\sigma$  can be calculated from the top of atmosphere (TOA) radiances using a coupled ocean-atmosphere radiative transfer model (RTM) simulating



one model run including ( $I^+$ ) and a second excluding ( $I^-$ ) inelastic processes:

$$\sigma = \ln\left(\frac{I^+}{I^-}\right). \quad (2)$$

For this study, three VRS fits were performed in three spectral regions 349.5 to 382 nm, 405 to 450 nm, and 450 to 493 nm, in the following referred to as UV, short-blue, and blue window, respectively. The blue and short-blue windows lie in TROPOMI's band 4, whereas the UV window lies in band 3. VRS fit factors have been successfully retrieved in the UV window using data from the GOME and SCIAMACHY sensor (Vountas et al., 2003, 2007). The blue window is slightly shorter than in Dinter et al. (2015) and Oelker et al. (2019), because TROPOMI's band 4 ends before 497 nm. VRS fits in the short-blue window are tested here for the first time. Considering all relevant processes in these fit windows for targeting VRS, the DOAS equation can be formulated as:

$$\tau(\lambda) = \ln \frac{I_0(\lambda)}{I(\lambda)} = \sum_{j=1}^J S_{a,j} \sigma_{a,j}(\lambda) + S_{VRS} \sigma_{VRS}(\lambda) + S_{OC} \sigma_{OC}(\lambda) + S_R \sigma_R(\lambda) + \sum_{m=0}^M x_m \lambda^m. \quad (3)$$

with atmospheric absorption cross sections  $\sigma_{a,j}(\lambda)$  of  $J$  atmospheric absorbers and pseudo-absorption cross section  $\sigma_R(\lambda)$  for Rotational Raman Scattering (RRS) in the atmosphere based on Equation (2). The pseudo-absorption cross section for VRS ( $\sigma_{VRS}$ ) was calculated based on Equation (2) from modeled case I TOA radiances for Chla of 0.1 mg/m<sup>3</sup> and a solar zenith angle (SZA) of 40° (see **Figure 2**, for more details on RTM setup see Section 2.3.2). This reference cross section describes the effect at the TOA of spectral redistribution due

to VRS at Chla of  $0.1 \text{ mg/m}^3$  (reference spectra simulated for other Chla are presented in **Supplementary Figure 1A**). VRS fit factors ( $S_{VRS}$ ) at this Chla are equal to 1.0 since a linear relationship is obtained between VRS fit factors and Chla around  $\text{Chla} = 0.1 \text{ mg/m}^3$  (compare **Supplementary Figure 1C**). The ocean weighting function ( $\sigma_{OC}$ ) was defined as in Dinter et al. (2015) and calculated from case I TOA radiances for a SZA of  $40^\circ$ . The weighting function describes the change in TOA radiance caused by a small change in Chla. It was calculated for a change in Chla from  $0.1 \text{ mg/m}^3$  to  $0.11 \text{ mg/m}^3$ . For the blue and short-blue window, the following atmospheric absorbers ( $a, j$  with  $J = 4$ ) were fitted: absorption cross sections for ozone ( $\text{O}_3$ ) (Serdyuchenko et al., 2014), nitrogen dioxide ( $\text{NO}_2$ ) (Vandaele et al., 1998), water vapor ( $\text{H}_2\text{O}$ ) (Rothman et al., 2013, using HITRAN 2009), and oxygen dimer ( $\text{O}_4$ ) (Thalman and Volkamer, 2013). The VRS fits in the blue and short-blue window only differ in wavelength region, whereas the UV window fit additionally differs in fitted atmospheric absorbers. In the UV window, the absorption cross section for bromine monoxide ( $\text{BrO}$ ) was additionally fitted, but water vapor was removed from the list of absorbers. For all three fit windows, a second order polynomial was chosen ( $M = 2$ ) which accounts for all broad band effects such as elastic scattering in atmosphere and ocean and aerosol, colored dissolved organic matter (CDOM) and non-algae particle absorption. Equation 3 is solved for the fit factors  $S$  for the fitted targets ( $OC$ , VRS, RRS and each atmospheric absorber) and the polynomial coefficients  $x_m$  using least-squares minimization (Richter, 1997).

### 2.3.2. RTM SCIATRAN

The coupled ocean-atmosphere RTM SCIATRAN (Blum et al., 2012; Rozanov et al., 2014, 2017, <https://www.iup.uni-bremen.de/sciattran/>) version 4.0.8 was used for radiance simulations for calculating pseudo-absorption cross sections and LUTs. Two types of RTM simulations have to be performed for the LUTs used to convert VRS fit factors to  $K_d$ . On the one hand, top-of-atmosphere (TOA) radiances, and on the other hand, underwater radiant fluxes for various ocean scenarios are needed. 23 different case-1 scenarios (Morel and Maritorena, 2001) were modeled with Chla ranging between 0 and  $30 \text{ mg/m}^3$ , i.e., optical properties of the ocean are driven by Chla, other optically active constituents such as CDOM change proportionally. Similar to the case-1 model in Hydrolight (Mobley and Sundman, 2013), the phytoplankton absorption spectrum (Prieur and Sathyendranath, 1981) was extrapolated into the UV range as an exponentially decaying function leading to a CDOM-dominated UV case-1 model. A background maritime aerosol was assumed with aerosol optical depth (AOD) of 0.1 at 550 nm. Detailed model settings can be found in Oelker et al. (2019) adapted from Dinter et al. (2015).

SCIATRAN can accurately model inelastic scattering processes such as VRS which was evaluated by comparison with other radiative transfer models and experimental data from satellite, ship-based, and underwater instruments (Rozanov et al., 2017). The VRS implementation is based on the parameterization of Haltrin and Kattawar (1993) in which the VRS emission is a sum of four Gaussian functions based on experimental results of Walrafen (1966) for a water temperature of  $30^\circ \text{ C}$  (note: the

temperature dependence of VRS has so far not been implemented in SCIATRAN). The total Raman scattering coefficient is set to a value of  $2.7 \cdot 10^{-4} \text{ m}^{-1}$  at a reference wavelength of 488 nm. The wavelength dependence is parameterized as a resonance model. Details on the VRS parameterization can be found in **Appendix A** of Rozanov et al. (2017).

TROPOMI-specific adaptations were made for this study. Since spectral alignment is very important for the DOAS retrieval, a TROPOMI-measured extraterrestrial solar spectrum was used for the TOA radiance calculations. A solar spectrum measurement from a middle row of the charge-coupled device (row 225, 0-based) from May 2018 was chosen. Underwater fluxes were simulated at a spectral resolution of 0.5 nm using a Fraunhofer atlas (Chance and Kurucz, 2010) since they are insensitive to the exact spectral resolution. Geometry settings were chosen to cover all of TROPOMI's viewing geometries [ $5^\circ$  steps for SZA and viewing zenith angle (VZA)], except for the azimuth angle which was held constant ( $90^\circ$ ).

### 2.3.3. Look-Up-Table for Deriving $K_d$ From VRS

Following Dinter et al. (2015), Oelker et al. (2019), the LUT for deriving  $K_d$  from VRS was built by combining VRS PhytoDOAS fits on simulated TOA radiances with  $K_d$  calculated from simulated underwater radiant fluxes. PhytoDOAS fit settings for the retrieval of theoretical VRS fit factors from the modeled TOA radiances are the same as for the retrieval on satellite radiances (see Section 2.3.1) except that for atmospheric cross sections water vapor was not fitted, since it was not included in the SCIATRAN simulation. The underwater radiant flux simulations provide the downwelling irradiance ( $E_d$ ) at discrete depths  $z$ . Taking into account the wavelength shift of the VRS process (Dinter et al., 2015),  $E_d(z, \lambda)$  was integrated over the specific VRS excitation wavelength range: for VRS-UV between 312.5 nm and 338.5 nm (UVAB), for VRS-short-blue between 356.5 nm and 390 nm (UVA), and for VRS-blue between 390 nm and 423 nm (blue). Then, according to Equation 1, the  $E_d(z, \text{UVAB})$ ,  $E_d(z, \text{UVA})$ , and  $E_d(z, \text{blue})$  were used to calculate the mean  $K_d(\text{UVAB})$ ,  $K_d(\text{UVA})$  and  $K_d(\text{UVAB})$ , respectively, until the first optical depth (see **Supplementary Figure 1**). The first optical depth, as defined by Gordon and McCluney (1975), was determined *via* linear interpolation of the log-transformed  $E_d(z)$ .  $K_d$  calculations and VRS PhytoDOAS retrievals were performed for each SZA and each VZA separately, an example for VRS-blue and  $K_d$ -blue is shown in **Supplementary Figures 1C,D**. VRS fit factors were matched with  $K_d$  calculated from scenarios with the same Chla. As an update to the two-dimensional LUTs in Dinter et al. (2015), Oelker et al. (2019), for each spectral  $K_d$  its specific, three-dimensional LUT was created where  $K_d$  is a function of VRS fit factor, SZA, and (newly added) VZA (see **Supplementary Figure 2**).

We note here that the LUT approach used in this study does not restrict the retrieval to ocean scenarios which correspond exactly to the chosen RTM parameterization. For instance, increased CDOM absorption with respect to a reference Chla value will lead to a reduction in VRS signal and, consistently, a lower  $K_d$  will be derived. Since this change in CDOM is, however, connected with a change in spectral shape of the VRS pseudo-absorption spectrum, the conversion to  $K_d$  *via* the LUT

can lead to errors. The retrieval sensitivity with respect to the RTM model settings was therefore investigated next.

### 2.3.4. Sensitivity Analysis

The algorithm sensitivity was evaluated with respect to model settings similar to the sensitivity analysis for  $K_d$ -blue retrievals presented in Oelker et al. (2019). Besides also considering the sensitivity of retrievals of  $K_d$ -UVAB and  $K_d$ -UVA, we extend the sensitivity analysis to the following parameters: CDOM spectral slope, UV-absorbing pigments, liquid water absorption, wind speed, and ozone concentration.

For each parameter, the sensitivity is analyzed as follows. An RTM simulation is performed to calculate radiances and radiant fluxes in which one parameter is increased or decreased with respect to the standard scenario used to build the LUT. The PhytoDOAS fit is performed on this modified scenario. Resulting VRS fit factors are converted to  $K_d$  using the LUT. The resulting  $K_d$  is compared to the expected value,  $K_d^{\text{exp}}$ , calculated from the radiant fluxes of the modified scenario. The deviation of derived from expected  $K_d$  is determined in percent.

Since mainly only a change in inherent optical properties changes  $K_d$ , the parameters can be separated into two groups. One group comprises the atmospheric and surface parameters which have no or only a minimal effect on the mean  $K_d$  over the first optical depth, but may influence VRS. The second group comprises the oceanic parameters which affect both,  $K_d$  and VRS. For the second group,  $K_d$  changes can be large, however, VRS changes accordingly, and  $K_d$  may be retrieved correctly within an uncertainty which is only a fraction of the change in  $K_d$ .

Parameters within the first group were varied as follows: wind speed was reduced to 1 m/s and increased to 8 m/s (standard: 4.1 m/s); aerosol optical depth (AOD) was reduced to 0.05 and increased to 0.2 (standard: 0.1); ozone profile was changed to one with reduced ozone concentration of 290 DU (standard: 420 DU).

The case-I assumption is generally not valid in the UV domain. The absorption coefficient can not be accurately described using Chla (Vasilkov et al., 2002a; Morel et al., 2007a). The influence of the case-I parameterization used for the optical constituents in the ocean on the ultraviolet  $K_d$  retrievals needs to be checked carefully. Case-I parameterization for the visible wavelength range were used in combination with a recent pure water absorption spectrum accurately measured for UV wavelengths (Mason et al., 2016). Nevertheless, the influence of the choice of water absorption spectrum is checked. A modified scenario is simulated with liquid water absorption coefficients from Pope and Fry (1997) which significantly differ at short wavelengths from those measured by Mason et al. (2016). High uncertainty also lies within the settings for phytoplankton and CDOM absorption. Presence of mycosporine amino acids (MAA) causes higher UV absorption than prescribed in our standard case-I parameterization. MAA absorb between 320 and 350 nm with a peak around 330 to 340 nm (Bracher and Wiencke, 2000). Presence of these UV-absorbing pigments should therefore mainly influence  $K_d$ -UVAB. A modified scenario was simulated using a phytoplankton absorption spectrum with medium MAA absorption (S9 from Bracher and Wiencke, 2000). High variability can also be expected for the

CDOM spectral slope, 0.01 to 0.03  $\text{nm}^{-1}$  (Vodacek and Blough, 1997) as compared to 0.014  $\text{nm}^{-1}$  in the standard case-I scenario. Modified RTM simulations were made with a reduced CDOM spectral slope of 0.007  $\text{nm}^{-1}$  and an increased CDOM spectral slope of 0.03  $\text{nm}^{-1}$ . Also the CDOM coefficient was modified as in Oelker et al. (2019), while keeping the CDOM spectral slope at 0.014  $\text{nm}^{-1}$ .

### 2.3.5. Offset Correction

TROPOMI-VRS blue fit factor range was higher than the range obtained when PhytoDOAS was applied to the simulated TOA radiances for constructing the LUTs. This resulted in a high bias of derived TROPOMI  $K_d$ -blue compared to matchup  $K_d$ -blue data from *in-situ* which indicated an offset between the measurement reality and the model, necessitating an empirical offset correction. The exact origin of the offset is so far unknown (discussed in Section 4.1), however, such global offsets are often observed in DOAS retrievals, especially for weak atmospheric absorbers, i.e., small signals (e.g., Wittrock et al., 2006; Platt and Stutz, 2008).  $K_d$ -blue agreed much better with the wavelength-converted  $K_d(490)$  from OLCI and OC-CCI when a constant was added to the VRS fit factors. Generally, TROPOMI  $K_d$ -blue is closer to the OLCI  $K_d$ -blue than the OC-CCI  $K_d$ -blue and correlation is highest for low  $K_d$  values (see Table 3). For developing an empirical VRS-fit offset correction, we concentrated on comparing the low values ( $K_d$ -blue < 0.15  $\text{m}^{-1}$ ) from the TROPOMI  $K_d$ -blue to those from the OLCI  $K_d$ -blue data set to determine the offset that best corrects the data. The comparison was calculated for the entire study time period using 5 min gridded daily  $K_d$  data as input. It covered a wide range of conditions (Chla 0.01 to 0.5  $\text{mg}/\text{m}^3$ , colored matter and phytoplankton absorption at 440 nm 0.003 to 0.05  $\text{m}^{-1}$  and 0.001 to 0.02  $\text{m}^{-1}$ , respectively, SZA 10° to 70° and VZA <60°). The offset correction of the VRS fit was optimized such that a linear total-least-square regression on this comparison data set (limited to  $K_d < 0.15 \text{ m}^{-1}$ ) yielded a slope close to one. The optimal offset was found to be 0.186. Regression statistics for this setting were a slope of 1.01, intercept of  $-0.002 \text{ m}^{-1}$ , and Pearson correlation coefficient of 0.80. The offset was used to correct all VRS fit factors and by that the whole  $K_d$  range. Details on the original  $K_d$ -blue data set and the applied correction can be found in the **Supplementary Material (Supplementary Figures 3, 4)**.

## 2.4. $K_d$ Product Quality Evaluation

$K_d$  products were evaluated against *in-situ* and multispectral  $K_d$  data sets. For all comparisons, we provide the slope and intercept of least-square regressions, the Pearson correlation coefficient, the bias, the mean absolute error (MAE), root-mean-square difference (RMSD), and the unbiased RMSD, calculated as  $\sqrt{\text{RMSD}^2 - \text{bias}^2}$ , as typical estimates used for ocean color variables (Brewin et al., 2015; Seegers et al., 2018).

### 2.4.1. Wavelength Conversion for $K_d(490)$

In order to compare our TROPOMI-derived  $K_d$  products to  $K_d(490)$  from OLCI and OC-CCI,  $K_d(490)$  needs to be wavelength-converted first. The spectral relationship between  $K_d$ -blue,  $K_d$ -UVA,  $K_d$ -UVAB and  $K_d(490)$  was investigated based

**TABLE 1** | Linear least-square regression results for *in-situ*  $K_d$ -UVAB,  $K_d$ -UVA and  $K_d$ -blue compared against *in-situ*  $K_d(490)$  from 19 stations during PS113.

$K_d$	Slope $a$	Intercept $b$ [ $m^{-1}$ ]	Pearson correlation $r$
UVAB	2.57	0.012	0.84
UVA	1.58	0.000	0.93
Blue	1.40	-0.008	0.98

on the *in-situ*  $K_d(\lambda)$  from 19 stations of PS113.  $K_d$ -blue,  $K_d$ -UVA,  $K_d$ -UVAB were determined from the *in-situ*  $K_d(\lambda)$  by averaging over the corresponding wavelength ranges. They were then plotted against the *in-situ*  $K_d(490)$ . Linear regression results can be found in **Table 1**. There is a tight relationship between  $K_d$ -blue and  $K_d(490)$ . Correlation with  $K_d(490)$  decreases with decreasing wavelength. Based on these results, OLCI and OC-CCI  $K_d(490)$  were wavelength-converted using

$$K_d\text{-blue} = a \cdot K_d(490) + b \quad (4)$$

with slope  $a$  and intercept  $b$  from **Table 1**.

### 2.4.2. Match-Up Analysis

Match-ups between geolocation of PS113 stations and TROPOMI ground pixels were calculated using a loose criterion given the low number of stations ( $N = 19$ ). We searched for each station for TROPOMI match-ups within  $\pm 2$  days and a radius of 5.5 km. If several match-ups were found in this time period, the match-up closest in time to the satellite measurement is taken. If more than one TROPOMI pixel lies within search criteria, the mean TROPOMI  $K_d$  was calculated and the standard deviation was noted as uncertainty of the TROPOMI  $K_d$ . Using this loose criterion, match-ups were found for 8 stations. OLCI and OC-CCI data were used to further quality control these 8 match-ups. The same spatial and temporal collocation criteria were applied to high-resolution OLCI data to find the corresponding OLCI data for each match-up. Following the Sentinel-3 ocean color validation protocol (EUMETSAT, 2021), OLCI match-ups were only considered valid if half of the pixel box was filled and if the coefficient of variation was not larger than 0.2. In addition, OC-CCI match-ups were determined with spatial collocation criterion of 1 by 1 (corresponding to TROPOMI criterion) and 3 by 3 pixel box to additionally check the spatial homogeneity as for OLCI. 7 of the TROPOMI match-ups were confirmed to be valid.

The same search criterion was applied to find match-ups between PS113 Triaxus and TROPOMI  $K_d$ . Again, the match-ups closest in time to the satellite measurement were selected and TROPOMI  $K_d$  is averaged in case more than one ground pixel lies within search radius. If several Triaxus measurements were matched with the same TROPOMI measurement, the Triaxus measurements were averaged and the standard deviation noted as variability in the Triaxus measurements, which indicates the spatial variability of the water mass. Thirty-five match-ups remain after averaging. Due to the focus of the oceanographic survey, Triaxus platform operations were taken to study the submesoscale variability, especially between different water

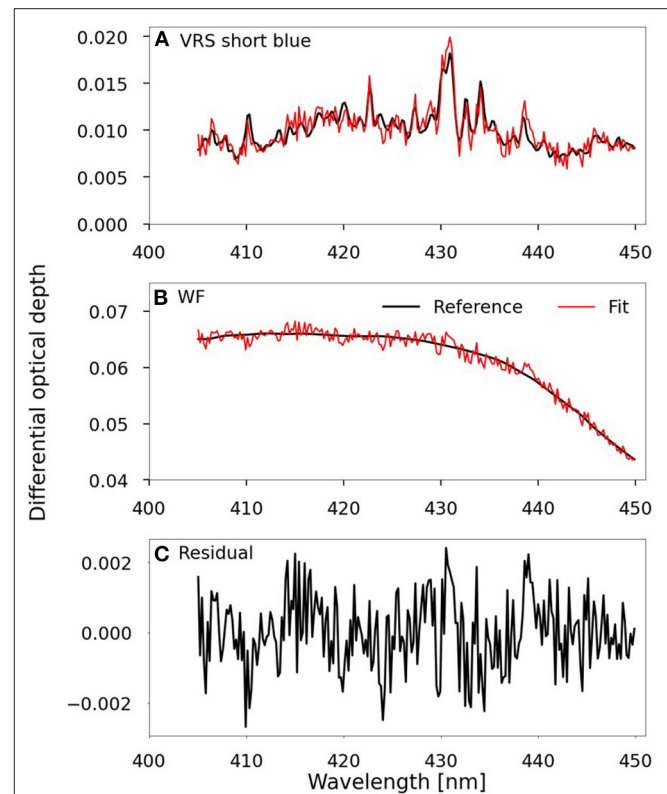


**FIGURE 3** | Differential optical depth for (A) VRS, (B) other oceanic parameters (oceanic weighting function - WF) and (C) overall fit residual of the spectral fit of TROPOMI TOA radiances using DOAS for the short-blue (405–450 nm) wavelength range for one pixel measured on 11 May 2018 at 16:02:37, 29.09°W, 32.12°S, at 59.56° SZA. For plots (A,B), the black line shows as reference the differential cross section multiplied by the retrieval fit factor for the corresponding ground pixel and the red line the reference plus the overall fit residual.

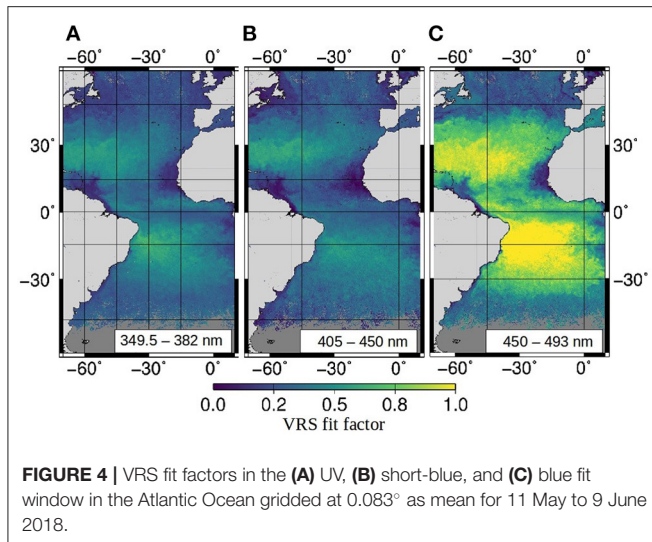
masses (as presented for a specific transect of the same cruise in von Appen et al., 2020). Since TROPOMI pixels are quite large, matchups with Triaxus data often show high innerpixel variability, while TROPOMI can only represent the mean value for the whole area.

## 3. RESULTS

We present for the three ranges of wavelengths the TROPOMI results of the VRS DOAS fits (section 3.1), the derived  $K_d$ -data which are also compared to *in-situ* and wavelength converted multispectral satellite  $K_d$  data (section 3.2), and the results of the sensitivity of the retrieval to parametrizations used in the RTM SCIATRAN (Section 3.3).

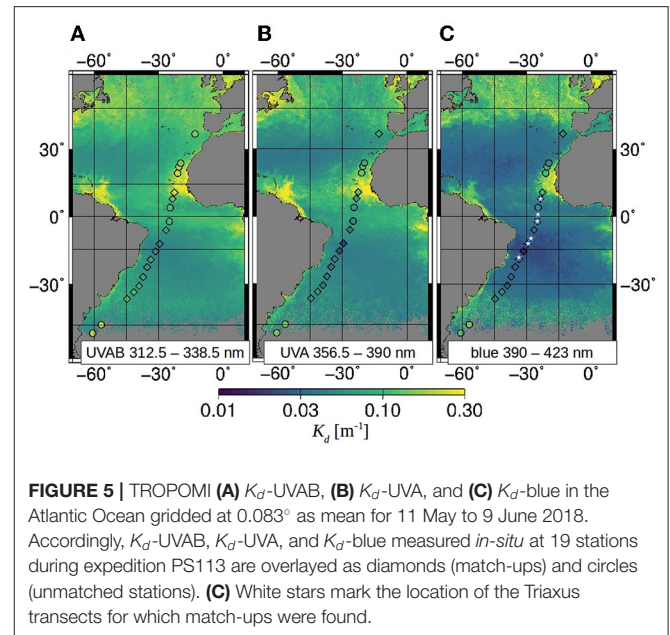
### 3.1. TROPOMI VRS DOAS Fits in the UV and Blue

The distribution of VRS fit factors, including fit residuals, for the three wavelength ranges were evaluated for the time period of the PS113 expedition in the Atlantic Ocean. **Figure 3**



shows an example of the differential optical depth for VRS, the ocean weighting function (second and third term in equation 3, respectively) and the VRS fit residual when the PhytoDOAS retrieval was applied to a TROPOMI ground pixel in the South Atlantic Gyre in the short-blue wavelength region. As expected for this region a strong VRS signal is obtained with the fit residual showing about 10% of this magnitude. Also the ocean weighting function is well-fitted with similar order of residual values. Similarly good fit results are obtained for the same pixel for the VRS fit in the UV and blue (see **Supplementary Figure 5**). This indicates that the signals from VRS and other ocean parameters are detected very well by the DOAS fit in the TOA radiances.

**Figure 4** shows a monthly composite of VRS fit factors for the three PhytoDOAS fit windows in the (**Figure 4A**) UV, (**Figure 4B**) short-blue, and (**Figure 4C**) blue in the Atlantic Ocean for the time period 11 May to 9 June. VRS fit factors in the blue window are presented offset-corrected. The data was gridded to 0.083° (~9 km). For all three fit windows, high and low VRS fit factors are found in typically low and high Chl<sub>a</sub> regions corresponding to low and high light penetration into the ocean, respectively. As expected, the VRS signal decreases with decreasing wavelength. Fit quality is similar for the PhytoDOAS fits in all three fit windows. The average root mean square (RMS) of all fit residuals in this area and time period and its standard deviation were evaluated to  $1.0 \cdot 10^{-3} \pm 3 \cdot 10^{-4}$  for the UV (excluding 26 outliers with  $\text{RMS} > 4$ ),  $0.9 \cdot 10^{-3} \pm 2 \cdot 10^{-4}$  for the short-blue, and  $1.0 \cdot 10^{-3} \pm 3 \cdot 10^{-4}$  for the blue fit window. For each ground pixel the fit error which is the relative uncertainty of the fit factor as determined from the linear least-squares DOAS fit, given in per cent, is provided. These errors (summarized in **Table 4**) are lowest for VRS-UV ranging from 5 to 10%, increased for VRS-short-blue to 10 to 15% and highest for VRS-blue with 15 to 20% within the given sensitivity range of  $K_d < 0.3 \text{ m}^{-1}$ , maximum errors for high  $K_d$ -/Chl-*a* waters are <20%, <40%, and <90%, respectively. VRS fit factors from



different fit windows are not strictly correlated, e.g., differences appear around Newfoundland and Great Britain.

### 3.2. TROPOMI $K_d$ Retrievals From the UV-B to the Blue

$K_d$  was pixel-wise derived from the TROPOMI VRS fit factors using separate LUTs for each wavelength region. **Figure 5** shows the resulting (**Figure 5A**)  $K_d$ -UVAB, (**Figure 5B**)  $K_d$ -UVA, and (**Figure 5C**)  $K_d$ -blue in the Atlantic Ocean gridded to 0.083° over the time period from 11 May to 9 June 2018. Lowest  $K_d$  are found in the North and South Atlantic Gyres, highest  $K_d$  in the upwelling regions along the African coast and the Amazon river plume. With decreasing wavelength,  $K_d$  increases. However,  $K_d$ -UVAB is not generally larger than  $K_d$ -UVA. In the upwelling regions off the coast of West African, the Amazon river plume, around Newfoundland, and around Great Britain the ratio  $K_d$ -UVA/ $K_d$ -UVAB is larger than 1 (roughly 1.25 on average, 2 in extreme cases).  $K_d$ -blue is strikingly larger than  $K_d$ -UVA and UVAB in the productive areas north of the Northern Atlantic Gyre.

Derived TROPOMI  $K_d$  products were compared to *in-situ*  $K_d$  measurements taken during expedition PS113. **Figure 5** shows the location of the PS113 stations and Triaxus transects. A rough correspondence between station  $K_d$  data and the satellite monthly mean  $K_d$  is already seen. For a direct comparison, match-ups between TROPOMI and *in-situ* data were evaluated. Match-ups for TROPOMI  $K_d$ -UVAB,  $K_d$ -UVA, and  $K_d$ -blue plotted against the corresponding *in-situ*  $K_d$  (**Figure 6**) show an overall good agreement for all three spectral wavelength regions, considering the loose match-up criterion. TROPOMI  $K_d$ -blue shows good agreement with the *in-situ*  $K_d$ -blue, which might not be so surprising since we offset-corrected the VRS fit factors for this wavelength range such that agreement is maximized for low  $K_d$ -blue with OLCI  $K_d$ -blue. Linear regression (**Table 2**) obtains

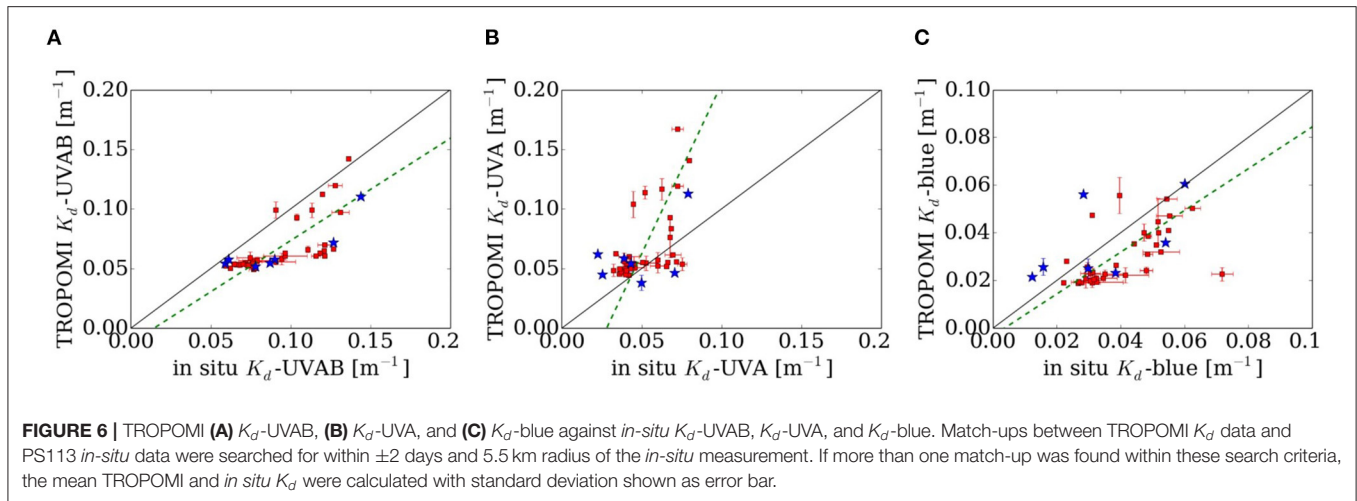


**TABLE 2 |** Metrics for the match-ups between TROPOMI against *in-situ*  $K_d$ -UVAB,  $K_d$ -UVA, and  $K_d$ -blue,  $N = 42$ .

$K_d$	$a$	$b$ [ $m^{-1}$ ]	$r$	Bias [ $m^{-1}$ ]	MAE [ $m^{-1}$ ]	RMSD [ $m^{-1}$ ]	Unbiased RMSD [ $m^{-1}$ ]
UVAB	0.86	-0.012	0.72	-0.026	0.026	0.031	0.017
UVA	2.85	-0.080	0.54	0.015	0.021	0.029	0.025
Blue	0.88	-0.003	0.54	-0.008	0.012	0.015	0.013

Given are slope  $a$  and intercept  $b$  from linear least-square regression, Pearson correlation coefficient  $r$ , bias, mean absolute error (MAE), and root mean square difference (RMSD).

a slope of 0.88 and an intercept of  $-0.003 m^{-1}$ . TROPOMI  $K_d$ -UVAB is systematically lower than the *in-situ*  $K_d$ -UVAB over the sampled  $K_d$  range (slope of 0.86 and an intercept of  $-0.026 m^{-1}$ ) with a bias of  $-0.026 m^{-1}$ . For TROPOMI  $K_d$ -UVA, an overestimation is observed that increases with  $K_d$ -UVA (slope of 2.85 and an intercept of  $-0.080 m^{-1}$ ). In line with this observation, bias, RMSD, and MAE are much lower for TROPOMI  $K_d$ -blue, and similar for  $K_d$ -UVAB and UVA except for the larger bias found for  $K_d$ -UVAB. Considering the unbiased RMSD, performance of TROPOMI  $K_d$ -blue and  $K_d$ -UVAB is similar and worse for  $K_d$ -UVA.

TROPOMI  $K_d$ -blue was compared to  $K_d$  data from the multispectral OLCI and OC-CCI data sets to evaluate random errors and regional differences between the data sets. For the latter,  $K_d(490)$  was converted to  $K_d$ -blue *via* a linear wavelength conversion scheme (Table 1). Since this wavelength conversion is principally valid for relating  $K_d(490)$  to  $K_d$ -blue, the comparison was restricted to  $K_d$ -blue and not extended to the UV  $K_d$ . For the study period and on the same grid as in Figures 4, 5, 7 shows  $K_d$ -blue for (Figure 7A) TROPOMI in comparison to (Figure 7B) OLCI and (Figure 7C) OC-CCI. Overall, TROPOMI  $K_d$ -blue patterns resemble the multispectral ones (e.g., gyres and productive areas around the Amazon river plume, Mauritanian upwelling system, English Channel). Regional differences are observed between TROPOMI and the multispectral  $K_d$ -blue, but also among the multispectral products. In the Atlantic gyres, OC-CCI  $K_d$ -blue is significantly higher than the other two products. Similar to OLCI, OC-CCI  $K_d$ -blue is lower in the North than in the South Atlantic Gyre, whereas TROPOMI

$K_d$ -blue is lower in the South. In the productive areas in the North Atlantic, the TROPOMI  $K_d$ -blue product appears noisier than the multispectral products. A distinct difference again is visible near Newfoundland. OLCI and OC-CCI show similar high- $K_d$  patterns north of Newfoundland whereas this pattern does not occur in the TROPOMI  $K_d$ -blue product. Around Great Britain,  $K_d$ -blue patterns from the multispectral products are not so similar to each other as those from OC-CCI compared to TROPOMI. Differences appear in maximum values south of  $40^\circ S$ , where SZAs are large and data coverage is low and differs between sensors. Despite these differences between the three data sets, comparison with RMSD (Figure 7D) as provided in the OC-CCI data set (converted to the blue spectral region) shows that these differences are on the order of the uncertainty of the OC-CCI product (see Supplementary Material for difference maps, Supplementary Figure 6).

All above mentioned data sets were gridded to  $0.083^\circ$  on a daily basis for the study period. Then, the satellite  $K_d$ -blue products were intercompared (TROPOMI vs. OLCI, TROPOMI vs. OC-CCI, and OLCI vs. OC-CCI) as well as the three TROPOMI  $K_d$  products among each other either based on the full data set or on a masked data set, where values above  $0.3 m^{-1}$  were excluded (Table 3). As can be seen from Figure 5, most satellite scenes are within this masked data set. Correlations between masked data sets are generally much larger than for full data sets. Significant correlation is found between TROPOMI  $K_d$ -blue and the multispectral  $K_d$ -blue, with slightly better agreement between TROPOMI and OLCI,  $r = 0.77$  for masked data set, than between TROPOMI and OC-CCI,  $r = 0.74$  for

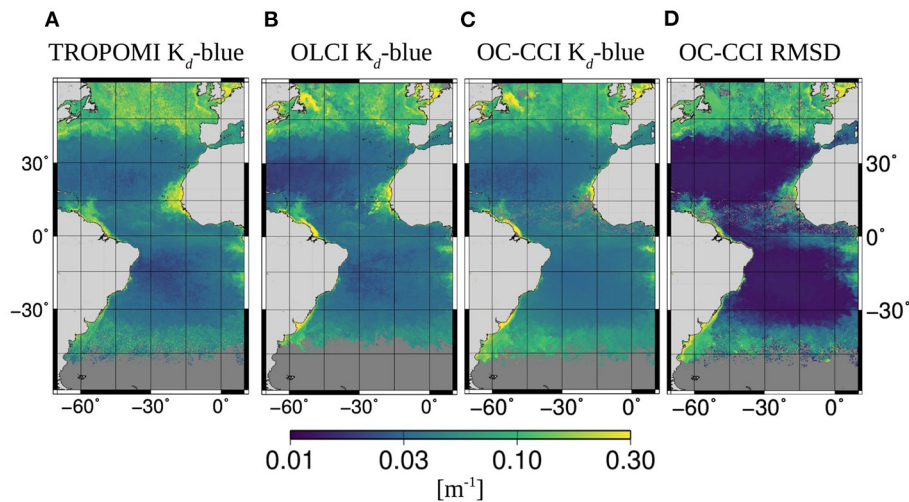


**FIGURE 7 | (A) TROPOMI, (B) OLCI, and (C) OC-CCI  $K_d$ -blue gridded at  $0.083^\circ$  as mean for 11 May to 9 June 2018. (D) RMSD provided in the OC-CCI product which was wavelength-converted to blue spectral range.**

**TABLE 3 | Comparison between TROPOMI against OLCI and OC-CCI  $K_d$ -blue,  $K_d$ -UVA and  $K_d$ -UVAB calculated on daily gridded data ( $0.083^\circ$ ) over time period 11 May to 9 June 2018.**

	$K_d$	Data set	$a$	$b$ [ $m^{-1}$ ]	$r$	Bias [ $m^{-1}$ ]	MAE [ $m^{-1}$ ]	RMSD [ $m^{-1}$ ]
TROPOMI vs. OLCI	Blue	Full	0.38	0.034	0.45	0.005	0.026	0.102
		Masked	1.02	-0.002	0.77	0.001	0.015	0.028
TROPOMI vs. OC-CCI	Blue	Full	0.57	0.021	0.45	0.004	0.022	0.076
		Masked	1.23	-0.015	0.74	0.003	0.015	0.027
OC-CCI vs. OLCI	Blue	Full	1.10	-0.004	0.68	0.002	0.015	0.085
		Masked	0.86	0.009	0.92	0.002	0.009	0.017
TROPOMI vs. TROPOMI	Blue vs. UVA	Full	1.01	0.019	0.44	0.020	0.039	0.073
		Masked	0.82	0.028	0.55	0.019	0.031	0.041
	Blue vs. UVAB	Full	0.69	0.054	0.53	0.037	0.051	0.071
		Masked	0.99	0.040	0.64	0.039	0.045	0.052

Given are slope  $a$  and intercept  $b$  from linear total-least-square regression, Pearson correlation coefficient  $r$ , bias, mean absolute error (MAE), and root mean square difference (RMSD).

masked data set. We note that the VRS fit factors underlying the  $K_d$ -blue product were corrected such that TROPOMI vs. OLCI yields a slope of one for an even smaller data set ( $K_d$ -blue <  $0.15 m^{-1}$ ). For the larger masked data set ( $K_d$ -blue <  $0.3 m^{-1}$ ), a slope of unity is still found. Higher correlation is found between the multispectral data sets ( $r = 0.92$ ). However, biases are observed depending on  $K_d$ -blue range. OC-CCI is larger than OLCI for small  $K_d$ -blue values, lower for medium  $K_d$ -blue values and again larger for the highest  $K_d$ -blue values in the data set. The hyperspectral UV  $K_d$  were only compared to TROPOMI  $K_d$ -blue and not to the multispectral data sets, since the wavelength conversion is less valid for the shorter wavelengths and the intercomparison indirectly contains information of the UV  $K_d$  with the multispectral products. The correlation between  $K_d$ -blue and  $K_d$ -UVA is lower than the

one between  $K_d$ -blue and  $K_d$ -UVAB, contrasting the finding on the relationship between the  $K_d$  from the *in-situ*  $K_d(\lambda)$ .

### 3.3. $K_d$ Retrieval Sensitivity

The overall retrieval performance was additionally evaluated through the sensitivity analysis with respect to chosen RTM settings. The varied atmospheric and surface parameters have a different influence on the filling-in by VRS as determined by Equation 2. The influence of AOD and wind speed is largest for the blue fit window and decreases with decreasing wavelength. It is negligible for wavelengths shorter than 360 nm. The influence of the ozone concentration is largest at the short wavelengths. It is negligible for wavelengths longer than 370 nm. Results for changes in AOD and wind speed were therefore only investigated

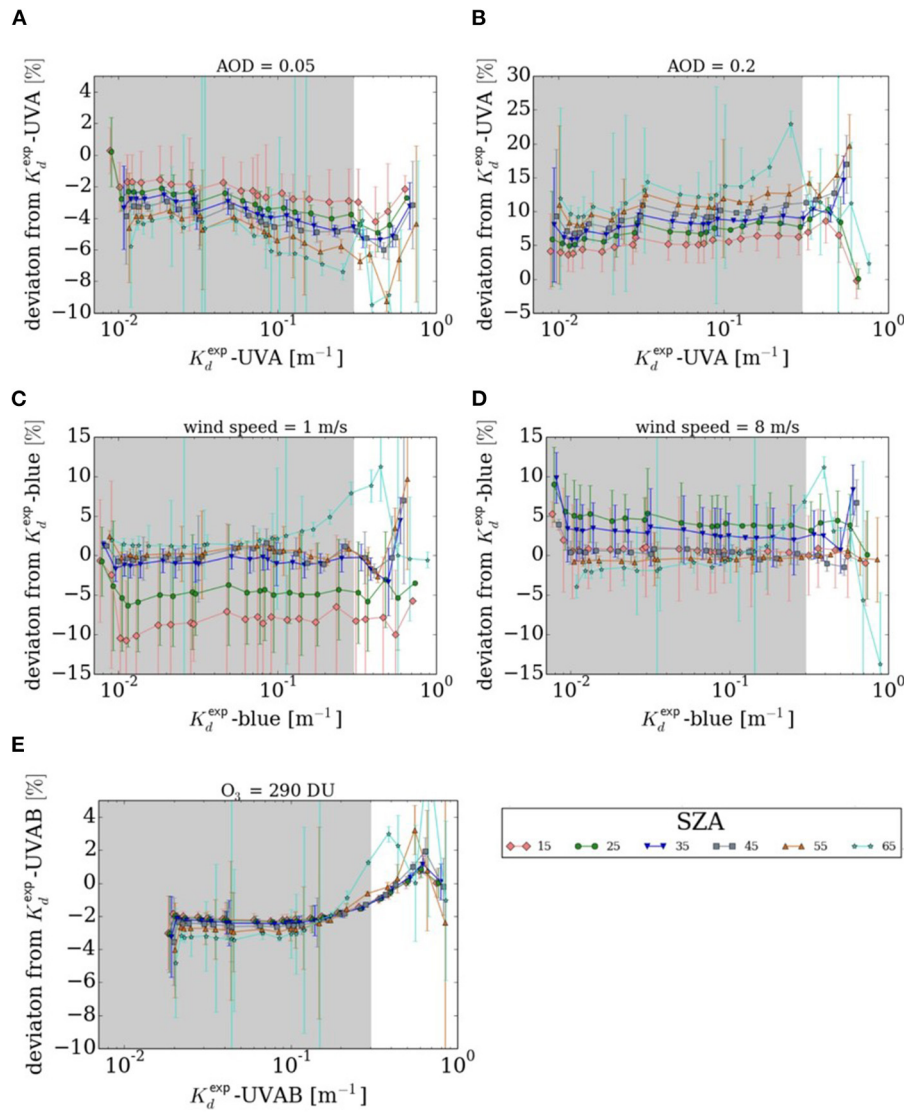


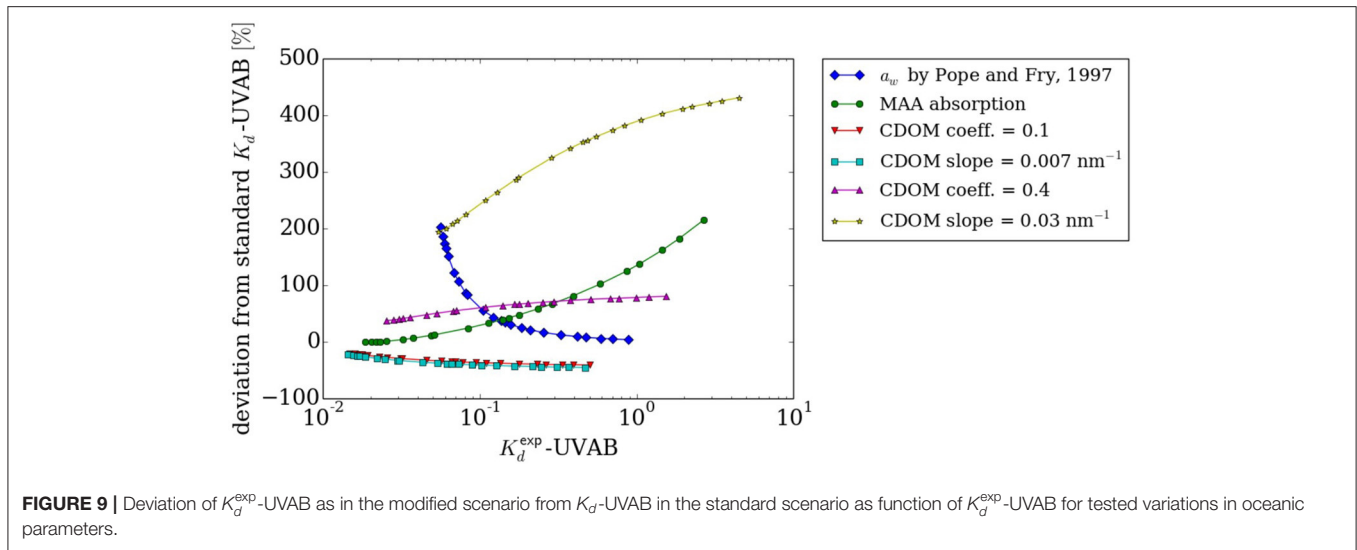
**FIGURE 8** | Deviation of derived from expected  $K_d$  in case of (A) reduced AOD, (B) increased AOD, (C) reduced wind speed, (D) increased wind speed, and (E) reduced ozone column for different SZA. Results were averaged for different VZA with the standard deviation given as errorbar. Panels (A,B) show results for  $K_d$ -UVA, (C,D) for  $K_d$ -blue, and (E) for  $K_d$ -UVAB.

for the short-blue and blue fit window and in ozone for the UV fit window (see **Supplementary Figure 6**).

The influence of aerosols on the  $K_d$ -blue retrieval was already presented in Oelker et al. (2019). A constant deviation over the  $K_d$ -blue range was found which was less than  $-5\%$  for the reduced AOD scenario and less than  $+20\%$  for the increased AOD scenario. **Figures 8A,B** show that the influence of aerosols on the  $K_d$ -UVA retrieval is similar in magnitude. The effect of aerosols on the  $K_d$ -UVAB retrieval (not shown) is significantly lower with only  $+5\%$  deviation for the increased AOD scenario. **Figures 8C,D** show the  $K_d$ -blue retrieval sensitivity with respect to wind speed. For most SZA, an altered wind speed causes deviations from the expected  $K_d$ -blue well below  $5\%$ . Larger deviations of up to  $\pm 10\%$  are found for specific SZA at the

lower SZA range ( $\leq 15^\circ$ ) depending on wind speed. The influence on  $K_d$ -UVA was even smaller as expected from the behavior of the filling-in by VRS. For the same specific SZA, deviations up to  $\pm 5\%$  can be found (not shown). The influence of the ozone column on the  $K_d$ -UVAB retrieval is below  $5\%$  shown in **Figure 8E**.

**Figure 9** shows the change in  $K_d$ -UVAB caused by the altered parameterizations with respect to the standard scenario, calculated as  $(K_d^{\text{exp}} - K_d^{\text{std}})/K_d^{\text{std}}$ . Implemented changes cause drastic changes in  $K_d$ -UVAB. The influence of the water absorption coefficients, MAA absorption, and a high CDOM spectral slope is especially large. For the clearest waters, the water absorption by Pope and Fry (1997) leads to an increase in  $K_d$ -UVAB by  $200\%$ . A similar increase is found for MAA



absorption for waters with highest Chla content. Since the reference wavelength for CDOM absorption is in the visible spectral region, an increase in CDOM spectral slope causes extreme changes in  $K_d$ -UVAB (about 200-430%). The other tested variations in CDOM parameterization in comparison lead to moderate changes in  $K_d$ -UVAB below 100%.

**Figure 10** shows retrieval sensitivity results for the oceanic parameters for  $K_d$ -UVAB. It can be seen that the retrieval performance is robust for  $K_d < 0.3 \text{ m}^{-1}$  which is highlighted in gray in **Figure 10**. This finding is in accordance with what we have seen in the comparison of  $K_d$ -blue with the multispectral data sets, the TROPOMI  $K_d$  can be well-retrieved for scenes with  $K_d < 0.3 \text{ m}^{-1}$ , discussed in Section 4.3. At higher  $K_d$  values, especially when considering MAA absorption and CDOM slope coefficients at high SZA ( $>60^\circ$ ) at high VZA ( $>65^\circ$ ), large error bars are obtained for the retrievals. This effect should be kept in mind, when the algorithm is applied in high latitudes. In the investigated Atlantic region, SZA are only moderately high and satellite pixels with high VZA are screened out by the cloud filter due to their larger pixel size. In the following, we focus on the  $K_d$  range below  $0.3 \text{ m}^{-1}$ .

The change in water absorption spectrum results in an overestimation of 15% for clear water scenarios which reduces to zero for high Chla scenarios, see **Figure 10A**. The overestimation is counter-intuitive, since  $K_d^{\text{exp}}$  is higher than  $K_d^{\text{std}}$ . A changed parameterization often also causes a spectral change in  $K_d$  which impacts the VRS fit quality and can result in this unexpected behavior. MAA absorption leads to an underestimation which increases to 20% at  $K_d$ -UVAB =  $0.3 \text{ m}^{-1}$  and can be significantly higher for higher  $K_d$ -UVAB (**Figure 10B**). A change in CDOM coefficient causes deviations of  $\pm 10\%$  (**Figures 10C,D**). A reduced CDOM spectral slope results in an overestimation of up to 20% and an increased CDOM spectral slope in an underestimation of up to 30% depending on Chla as shown in **Figures 10E,F**. The influence on the  $K_d$ -UVA retrieval was also evaluated with respect to water absorption and CDOM. Results

are qualitatively similar, however, the influence is generally smaller. Overestimation up to 10% for the change in water absorption, overestimation of up to 10% in case of reduced CDOM spectral slope, and underestimation up to 25% in case of increased CDOM spectral slope are found. A change in CDOM coefficients leads to similar deviations of  $\pm 10\%$ .

**Table 4** summarizes the maximum model errors to expect when not correctly parameterizing the oceanic and atmospheric parameters within the TROPOMI  $K_d$  algorithm.

## 4. DISCUSSION

### 4.1. VRS Retrievability

The VRS signal in TROPOMI-measured backscattered radiances can be successfully identified using DOAS. Spatial patterns of VRS fit factors are consistent with distribution patterns of Chla, the main driver for light attenuation in the open ocean. Absolute values of VRS fit factors retrieved from TROPOMI data are in reasonable agreement with those retrieved from simulated backscattered radiances shown by the successful conversion to  $K_d$  using the RTM-based LUTs. TROPOMI VRS fits are very sensitive which is proven by low fit residuals and errors. These are one order of magnitude lower than the results obtained with DOAS from older atmospheric sensors such as GOME, SCIAMACHY, GOME-2 and OMI (Vountas et al., 2003, 2007; Dinter et al., 2015; Oelker et al., 2019). Still, a source of systematic uncertainty could be that the VRS pseudo-absorption cross section compensates the VRS spectral features less well for Chla that substantially differ from the reference value since it is calculated for Chla of  $0.1 \text{ mg/m}^3$ . However, the LUT approach accounts for the variability of Chla, SZA and VZA, thereby lowering to a large extent this effect which we consider sufficient for this feasibility study. The quality of this approach could be further improved in the future by exploring iterative DOAS approaches (e.g., Richter, 2009). The conversion of TROPOMI

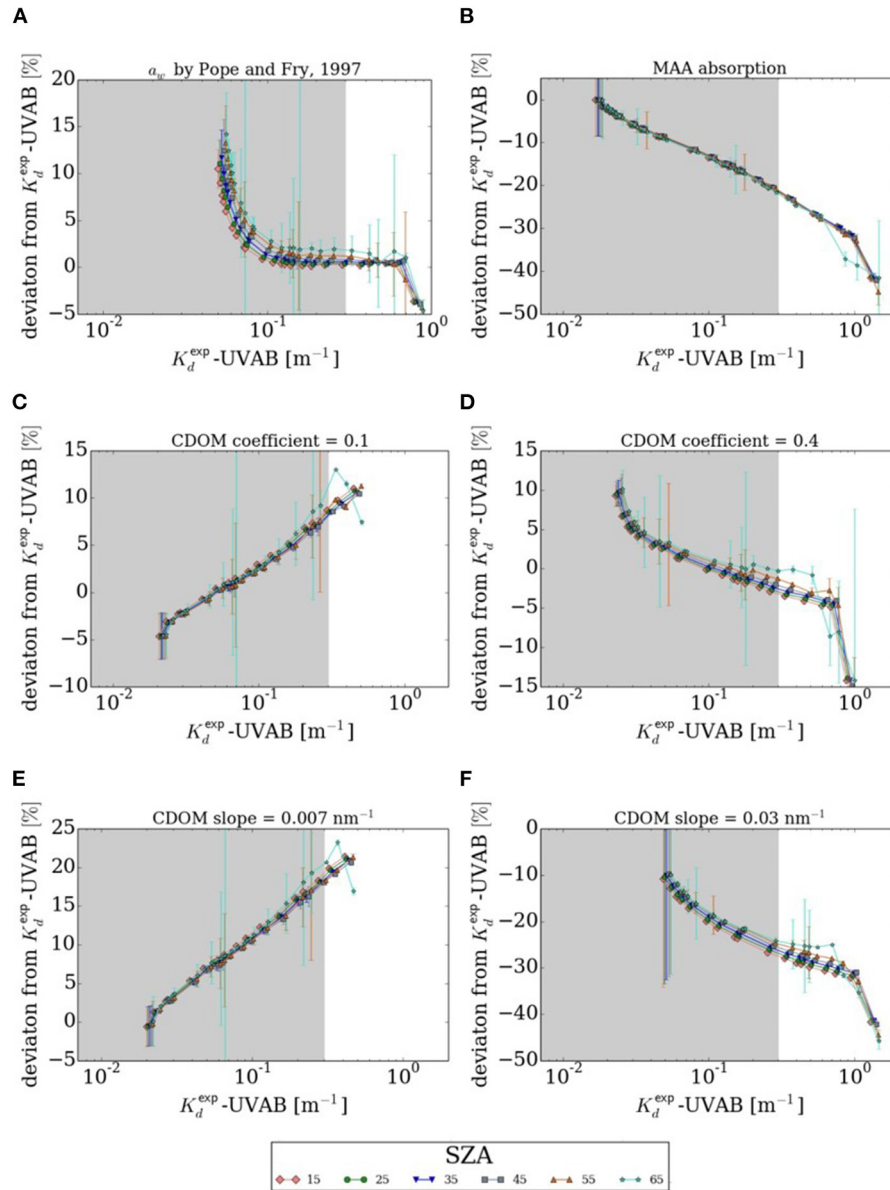


**FIGURE 10 |** Deviation of derived from expected  $K_d$ -UVAB in case of (A) liquid water absorption by Pope and Fry (1997), and (B) MAA absorption, (C) reduced and (D) increased CDOM coefficient, (E) reduced and (F) increased CDOM spectral slope as function of expected  $K_d$ -UVAB. Results were averaged for different VZA with the standard deviation given as error bar.

**TABLE 4 |** Maximum VRS fit (fit) and model errors provided in percent for the TROPOMI  $K_d$ -UVAB,  $K_d$ -UVA, and  $K_d$ -blue retrievals  $<0.3 \text{ m}^{-1}$ .

$K_d$	Fit	$a_{CDOM}$	CDOM-S	$a_{ph}^*$	AOD	WS	$O_3$
UVAB	10	10	30	20	5	3	3
UVA	15	10	25	20	15	5	0
Blue	20	20	25	10	20	10	0

Model errors are defined for not correctly parameterizing in the VRS cross section and LUTs RTM simulations the specific oceanic [CDOM absorption slope (CDOM-S) and coefficient ( $a_{CDOM}$ ), the phytoplankton absorption ( $a_{ph}^*$ )] and atmospheric parameters [aerosol optical thickness (AOD), wind speed (WS) and ozone concentration ( $O_3$ )]. They are based on the sensitivity studies presented in section 3.3 and Dinter et al. (2015).

VRS fit factors to  $K_d$  yielded better results for the UV and short-blue than for the blue fit window. A simple additive correction was necessary here.

The requirement of an additive correction factor that brings together retrieved fit factors with model predictions is a typical DOAS problem (Irie et al., 2015; Seo et al., 2019). Peters et al. (2014) pointed out that theoretical VRS pseudo-absorption spectra are not ideal for compensating VRS structures in actual DOAS measurements of clear waters. Such a mismatch could explain the requirement of a correction term. If this is the case, the effect of this mismatch on the DOAS retrieval is dependent on fit window, since we did not observe an obvious need for a correction of VRS fit factors in the short-blue and UV fit windows. Similar to this study, Oelker et al. (2019) have encountered discrepancies between retrieved VRS fit factors on satellite and simulated backscattered radiances for the sensors GOME-2, OMI, and SCIAMACHY. They managed to reduce this discrepancy by including cross sections in the DOAS fit for GOME-2 and SCIAMACHY which account for spectral features caused by instrumentation. The DOAS VRS fit on OMI data showed no sensitivity to empirical cross sections. We checked if such empirical cross sections calculated from fit residuals over cloudy scenes - which are essentially VRS-free scenes - improve the situation for TROPOMI. No impact on VRS fit factors was found. We therefore suggest a different reason for the required offset correction. While performing DOAS fits on simulated data, we observed a correlation with  $O_4$  that is strongest in the blue fit window, weaker in the short-blue fit window and weakest in the UV fit window. This correlation behaves differently for fits of actual satellite scenes. DOAS retrievals targeting  $O_4$  also often require additive correction factors, caused by an insufficient quality of the  $O_4$  absorption cross section (Spinei et al., 2015). The effect of  $O_4$  on the VRS retrieval should be further investigated to obtain a correction which is independent from other  $K_d$  products.

## 4.2. Ultraviolet $K_d$ Product Quality

We relied on *in-situ* match-up analysis to evaluate  $K_d$ -UV product quality, on which multispectral sensors do not provide any information. Match-up analysis was not feasible for older hyperspectral sensors due to large ground pixel sizes. Before TROPOMI was launched, OMI had the best spatial resolution with 13 km by 24 km at nadir. The spatial resolution has dramatically increased with TROPOMI to 3.5 km by 7 km at nadir in 2018. This is still a large pixel size for comparison with point measurements, yet our results show a decent agreement between match-ups of hyperspectral and *in-situ*  $K_d$ . Since the number of stations and transects was small, we used a loose criterion for searching for match-ups. The temporal discrepancy between satellite and *in-situ* data certainly adds uncertainty to the comparison, however, the *in-situ* data for which match-ups were found was sampled in regions with rather low temporal dynamics. A search criterion of  $\pm 2$  days is therefore certainly not ideal, but a good compromise. Match-ups with *in-situ* data were obtained within two different biogeochemical provinces, the South Atlantic Tropical Gyre (SATL) and the Western Tropical Atlantic (WTRA) according to Longhurst et al. (1995) (compare

Bracher et al., 2020). The evaluation of the  $K_d$  product quality is therefore restricted to the low  $K_d$  range. The discrete station data to derive diffuse attenuation has been obtained close to the ship and uncertainty introduced by residual reflection by the ship's hull may be large. We could not quantify this effect directly, however, it should be rather small: Within Bracher et al. (2020), using the same station and Triaxus  $E_d$  data of our study phytoplankton group Chla including an uncertainty assessment was derived. It showed a homogeneous data set with no differences between closely located station and Triaxus based data. Similarly, also for our *in-situ*  $K_d$  data, no significant difference in values between closely located station and Triaxus data was observed. We want to highlight that we claim the Triaxus data to be not at all influenced by the ship reflectance, since the radiometry installed on the Triaxus system is towed at a distance of  $>500$  m to the ship. Besides, our radiometric measurement set-up at the discrete stations has also been used within the international field intercomparison of radiometer measurements for ocean color validation in 2018. Results showed that measurements from this set-up was within 10% to the other radiometric measurement devices and AERONET-OC reference system in the blue wavelength region (Tilstone et al., 2020).

TROPOMI ultraviolet  $K_d$  products are promising as shown by comparison to *in-situ* data. Overall, there is good agreement between the TROPOMI and *in-situ*  $K_d$ . Quality of the *in-situ*  $K_d$  at short wavelengths is limited. The TriOS sensor only measures down to 320 nm and its measurement accuracy appears to decrease toward this lower end of the spectral range as observed also by other users (Nicolaus et al., 2010). Consequently, the *in-situ*  $K_d$ -UVAB has a spectral mismatch to the TROPOMI  $K_d$ -UVAB. Evaluated from the RTM simulations, the *in-situ*  $K_d$ -UVAB is expected to be about 5 to 10% lower than the satellite  $K_d$ -UVAB due to this spectral mismatch, which would imply an even larger underestimation of  $K_d$ -UVAB by TROPOMI. Potential biases of TROPOMI  $K_d$ -UVAB need to be checked in the future with high-quality radiometric measurements in the UV spectral range.

$K_d$ -UVAB at  $<1$  mg m<sup>-3</sup> Chla should be larger than  $K_d$ -UVA resulting from RTM (Dinter et al., 2015), considering that CDOM absorption decreases exponentially with wavelength. A decreasing  $E_d$  with decreasing wavelength in the UV is backed up by field data (Baker and Smith, 1982; Conde et al., 2000). An exception might be waters with extremely low CDOM concentrations for which hardly any difference was observed between  $K_d$  at 310 and 465 nm (Højerslev and Aas, 1991). However, the ratio between  $K_d$ -UVA and  $K_d$ -UVAB is larger than 1 for high- $K_d$  ( $>>0.3$  m<sup>-1</sup>) waters where we do not expect low CDOM concentrations. The multiplicative bias might be correctable by adding an offset to the VRS fit factors in the short-blue fit window similar to the offset correction performed for  $K_d$ -blue. We did not try to correct the VRS fit factors used to calculate  $K_d$ -UVA since no reference is available at the moment.

In addition to these systematic biases, spatial patterns differ between the two  $K_d$ -UV products. Daily comparisons of the gridded products with  $K_d$ -blue showed a lower correlation with  $K_d$ -UVA than with  $K_d$ -UVAB. This observation contrasts the analysis of the spectral relationships between  $K_d$  at different

wavelengths derived from the *in-situ*  $K_d(\lambda)$ . However, quality of the *in-situ* measurements decreases with wavelength, naturally causing the correlation coefficient to decrease with wavelength. Other studies found also a decreasingly robust relationship with wavelength between  $K_d$  in the UV range and optical properties in the VIS range (Johannessen et al., 2003; Vasilkov et al., 2005; Smyth, 2011). A very robust relationship between  $K_d$  at 310 and 465 nm with correlation 0.998 was found in low-CDOM waters (Højerslev and Aas, 1991). It is therefore not generally clear, how robustly the  $K_d$ -UV are related to  $K_d$ -blue in different parts of the ocean. Light attenuation in the UV is mainly determined by CDOM and mycosporine-like amino acid (MAA) absorption. Based on its origin, CDOM has different absorption characteristics. VIS absorption is much stronger for humic substances with less steep spectral slope as opposed to mostly protein degrading substances of marine origin (Nelson and Siegel, 2002).

MAA production depends on UV irradiation and species composition (Vernet et al., 1994) and mainly influences  $K_d$ -UVAB due to MAA absorption peaks at 330 to 340 nm (for influence on  $K_d$ -UVA, see also discussion in Wang et al., 2021). Presence of MAA should therefore mainly influence  $K_d$ -UVAB. Since the link between optical properties in different spectral regions of the UV-VIS is not robust from a biogeochemical perspective, it is necessary to directly infer spectral information on light penetration, highlighting the importance of this study. By covering three spectral regions, the TROPOMI  $K_d$  products can give insight on CDOM origin and MAA production. The algorithm sensitivity analysis has shown that the  $K_d$ -UV retrievals are only moderately sensitive to the chosen RTM parameterization (see further discussion in Section 4.4). Changes in  $K_d$ -UV caused by sufficiently large changes in CDOM and phytoplankton absorption should therefore be resolvable.

More *in-situ* data, covering a larger  $K_d$  range and of high quality in the UV spectral region, are necessary to thoroughly evaluate  $K_d$ -UV performance. A larger data set could then also be used for estimating if a correction term for  $K_d$ -UVA is necessary as well as for quantifying this correction term.

### 4.3. Blue $K_d$ Product Quality

TROPOMI  $K_d$ -blue agrees well with OLCI and OC-CCI  $K_d$ -blue. Differences between the TROPOMI, OLCI, and OC-CCI  $K_d$ -blue products are within the uncertainties given for the OC-CCI data set. Higher agreement between the two multispectral  $K_d$ -blue data sets than between multi- and hyperspectral ones has to be put into perspective, considering different ground pixel sizes of the sensors. In addition, a perfect correlation between multi- and hyperspectral products is not expected due to the uncertainty associated with the wavelength conversion. We therefore want to stress the importance of direct retrievals of  $K_d$  at other wavelengths. However, we are confident that the comparison between the hyperspectral and multispectral  $K_d$ -blue is robust in the oligotrophic waters of our study area because wavelength conversion was calculated from *in-situ* data measured in exactly these waters in the time period of the study. Evaluating the offset correction term from comparison with OLCI  $K_d$ -blue for small values ( $K_d$ -blue  $< 0.15 \text{ m}^{-1}$ ) is meaningful. Systematic

biases between the data sets cannot be evaluated independently, but comparing them was possible with respect to regional differences, discrepancies for  $K_d$ -blue values above  $0.15 \text{ m}^{-1}$ , and random errors.

$K_d$ -blue product quality is especially good in most of the open ocean, but reduced in areas where  $K_d$ -blue  $> 0.3 \text{ m}^{-1}$  which covers less than 5% of the world's ocean. Oelker et al. (2019) pointed out that the strength of the hyperspectral algorithm lies in low- $K_d$  waters since the VRS signal is highest here. The retrieval sensitivity decreases with increasing  $K_d$ . In some cases, the hyperspectral algorithm seems to fail for high- $K_d$  scenes causing obvious regional discrepancies in the TROPOMI  $K_d$ -blue product, as in the waters around Newfoundland, as compared to the multispectral sensor values. Not only the general retrieval sensitivity plays a role for the performance in productive areas, also the model setup. Because we set up our model for case-I waters, our  $K_d$ -blue product is only valid for open ocean scenarios. For coastal applications, the model has to be adjusted accordingly. The multispectral algorithms have already been adapted for high- $K_d$  waters. The semi-analytical algorithm by Lee et al. (2005b) has shown to perform well in coastal areas (Lee et al., 2005a) and inland waters (Gomes et al., 2018) whereas the OK2-555 algorithm by Morel et al. (2007b) only covers case-I waters.

The TROPOMI  $K_d$ -blue product outperforms other hyperspectral  $K_d$ -blue products. The product quality is higher in more productive waters than for SCIAMACHY, OMI, and GOME-2. Oelker et al. (2019) limited the  $K_d$ -blue products from these three older hyperspectral sensors to below  $0.15 \text{ m}^{-1}$ . For these reduced data sets, correlations with OC-CCI  $K_d$ -blue around 0.65 were achieved. Since their metrics are given for daily comparisons of almost 1 year of data, we cannot compare our monthly metrics one to one. However, TROPOMI  $K_d$ -blue correlation with the multispectral  $K_d$ -blue is above 0.7 for the reduced data set including values up to  $0.3 \text{ m}^{-1}$ . The scatter plots presented in Oelker et al. (2019) show that the hyperspectral  $K_d$ -blue already diverges from the OC-CCI  $K_d$ -blue in this  $K_d$  regime. Partially, this improvement is caused by the much lower ground pixel size of TROPOMI, which is closer to the multispectral satellite footprints, and thus reduces the representation error between the data sets. Smaller ground pixel sizes also reduce the inhomogeneity in satellite scenes improving fit quality. The improved DOAS fit quality of TROPOMI compared to its heritage sensors has also been found for UV-VIS retrievals of atmospheric trace gases (Seo et al., 2019; van Geffen et al., 2020). The spread in the scatter plots appearing as a “butterfly shape” was first observed by Dinter et al. (2015) for SCIAMACHY and has appeared in all comparisons between hyper- and multispectral  $K_d$  products so far (see **Supplementary Material** for TROPOMI scatter plots, **Supplementary Figure 4**). A systematic difference in the method or sensor measurement technique seems to cause a behavior where multispectral data see high  $K_d$  values for scenes for which the hyperspectral  $K_d$  is low and vice versa. Hardly any high- $K_d$  scenes occur in the data sets where hyper- and multispectral  $K_d$  are in agreement. This behavior was discussed in Dinter et al. (2015) and Oelker et al. (2019) and attributed to low

retrieval sensitivity for high- $K_d$  scenes causing one wing of the distribution and to cloud contamination and large deviations from the average ocean scenario prescribed in the model causing the other wing.

#### 4.4. TROPOMI $K_d$ Products Uncertainty

When specifying the uncertainty of the retrieved VRS fit factor and derived  $K_d$  retrievals, several effects have to be taken into account.

Photon-shot noise, related to the number of photons collected in a single measurement and governed by the probability distribution of incoming photons (Burrows and Borrell, 2011), together with readout noise and the detector's dark signal, are the main sources of random errors in the radiance measurements.

Systematic errors in the VRS fit factors are introduced by an imperfect wavelength calibration and other instrumental features not fully calibrated for in the TROPOMI Level-1 data calibration (e.g., Ludewig et al., 2020) and uncertainties in the reference spectra of all considered atmospheric absorbers, RRS, VRS and oceanic weighting function. The uncertainties in the reference spectra are propagated into the conversion of the VRS fit factor into  $K_d$ . The LUTs, used for the conversion, further introduce systematic uncertainties by not fully representing atmospheric and oceanic optical properties. In addition, the presence of clouds could lead to significant uncertainties in satellite retrievals.

Within our retrieval the errors introduced by clouds can be considered as marginal as we apply a strict cloud filtering. The VRS fit factor error represents random errors listed above and also includes most of the systematic errors considering imperfect wavelength calibration, instrumental effects and uncertainties in the reference spectra. The results from the retrieval sensitivity studies (provided in Section 3.3, Dinter et al., 2015; Oelker et al., 2019) as quantitative assessment of the TROPOMI  $K_d$  uncertainty give information on the systematic errors introduced by specific settings of the parametrizations in SCIATRAN related to LUTs to convert the VRS fit factor into the  $K_d$  value which are discussed in the following.

The influence of atmospheric and surface parameterizations on the TROPOMI  $K_d$  retrievals can be considered generally low. Uncertainties increase with the difference between conditions found for an actual satellite scene and the average ones used in the simulated standard scenario. Largest uncertainties can be expected for scenes with high aerosol loadings, which only occur in specific regions and times of the year (Remer et al., 2008). For the Atlantic region, Saharan dust storms can have a significant influence (e.g., van der Does et al., 2016). Maritime aerosols were investigated here while terrestrial dust might have even stronger impacts. However, these critical scenes are largely removed through the strict cloud filter criterion used in the retrieval (cloud fraction of 0.01). We conclude that the here presented LUT presents a solid basis for  $K_d$  retrievals in the blue and UV spectral range. Compared to other semi-analytic approaches, the degree of assumptions made is similar. For instance, RTM simulations for the  $K_d$  method by Lee et al. (2005a) were also made for a mean global wind speed. Nevertheless, to further enhance the quality of the LUT-derived  $K_d$  in the future, the dimensionality of the LUT can be further increased to include aerosol loading, wind

speed, and ozone column as input parameters that can be taken from ancillary data sets with sufficient quality. Parameters like aerosol optical depth and ozone column are even provided by the TROPOMI sensor.

With respect to the oceanic parameters, the TROPOMI  $K_d$  retrievals are rather insensitive to the chosen RTM parameterization compared to the large variability that this parameterization causes in  $K_d$  in the UV spectral range. The analysis in this study focused on the UV spectral range for two reasons: (1) the influence of oceanic parameterization on the  $K_d$ -blue was already discussed in Dinter et al. (2015) and Oelker et al. (2019) and (2) parameterization in the UV spectral range is less straight forward since a simple parameterization with Chla as used in the visible region for case I waters is not suitable (Vasilkov et al., 2002b; Morel et al., 2007a). As demonstrated by the sensitivity analysis, the exact oceanic RTM parameterization is not of importance since a change in oceanic parameter causes a change in  $K_d$  and VRS. The uncertainties of derived  $K_d$  for scenes with large differences to the reference RTM scenario are only a fraction of the change in  $K_d$  for these scenes. The sensitivity analysis results underline the robust retrievability of  $K_d$  in the UV spectral range using DOAS VRS-fits in combination with a LUT-based approach, as it had been found for  $K_d$ -blue in Dinter et al. (2015) and Oelker et al. (2019).

$K_d$  retrievals from OC sensors show low uncertainties for the visible spectral range. For the semi-analytical OC-CCI  $K_d(490)$  algorithm, Lee et al. (2005b) report that for 90% of the retrieved  $K_d(490)$  are within 25% of the *in-situ* measurement. It is not yet clear if similar quality can be reached for estimation of  $K_d$ -UV from the UV bands of current OC sensors or the UV wavelengths of the upcoming PACE mission. Due to lower intensity of the solar radiation in the UV, UV measurements are generally closer to the noise level. Also, atmospheric correction is more challenging at these short wavelengths (Frouin et al., 2019). Indirect retrievals of  $K_d$ -UV from OC bands at visible wavelengths have also shown decent performance. For instance, Fichot et al. (2008) obtain  $K_d(380)$  with mean relative error of about 10% and  $K_d(340)$  and  $K_d(325)$  with mean relative error around 18% from validation with 72 *in-situ* match-ups. They note that presence of MAA can cause larger errors on their retrieval at the shorter wavelengths. Because of the loose relationship between the spectral range below 360 nm and the visible, (Wang et al., 2021) do not apply their neural network approach in this spectral range. We stress that a direct approach, analyzing the radiation backscattered in the UV wavelengths, should be further pursued to obtain  $K_d$  below 360 nm. In addition, the algorithm presented in this study provides an independent approach which can be used as verification for the  $K_d$  products from typical OC sensors which is especially important for the to date presented indirect  $K_d$ -UV OC data which are based on highly empirical approaches. Regions where empirical relationships might not hold are potentially identified.

Since the TROPOMI data acquisition started in May 2018, *in-situ* radiance measurements of underwater profiles have been very limited. The current *in-situ* matchup data set is too small to be included in a comprehensive error budget evaluation for our TROPOMI  $K_d$  retrievals. We use the maximum retrieval errors

based on the relative VRS fit error (see discussion in Section 4.1) and the results from the retrieval sensitivity studies (provided in Section 3.3 and Dinter et al., 2015) as quantitative assessment of the TROPOMI  $K_d$  uncertainty (see Table 4). More precise calculations of the total error of the  $K_d$  retrieval are currently not possible since we do not know the distribution function of the optical and atmospheric constituents in the atmosphere and ocean. In addition, the uncertainty which is introduced for the  $K_d$  retrieval by the VRS offset correction is not quantified (see discussion in Section 4.1). We expect that the TROPOMI  $K_d$ -blue error (at least for  $K_d < 0.3 \text{ m}^{-1}$ ) will not be larger than those provided for OC-CCI. This is based on the rather low theoretical retrieval uncertainties, the low relative VRS fit factor errors and that for TROPOMI  $K_d$ -blue we obtained an agreement to the OC-CCI and OLCI  $K_d$  products within OC-CCI RMSD. Since  $K_d$ -UV retrievals even showed lower relative fit error and theoretical error for atmospheric parametrizations in SCIATRAN, we consider their total error to be similar or even lower.

## 5. CONCLUSION

We successfully exploited TROPOMI's UV-VIS bands for deriving  $K_d$  in the open ocean. This first application of TROPOMI data for oceanic retrievals yields promising results. Two novel  $K_d$  products in the UV [312.5 to 338.5 nm (UVAB) and 356.5 to 390 nm (UVA)] were presented showing plausible agreement with  $K_d$  *in-situ* data. In addition, a  $K_d$  product in the blue was retrieved (390 to 423 nm) that showed a better performance than  $K_d$ -blue from SCIAMACHY, GOME-2 and OMI in earlier studies.  $K_d$ -blue agrees well with the wavelength-converted  $K_d(490)$  products from the multispectral data sets OLCI and OC-CCI. Differences between the three  $K_d$ -blue products were found to be within the uncertainties of the OC-CCI data set.

The robust agreement of TROPOMI  $K_d$  products with multispectral data sets and the reasonable agreement with *in-situ* data show that VRS can be successfully retrieved using PhytoDOAS and converted to  $K_d$  using an RTM-based LUT. Several retrieval sensitivities were investigated in detail, leading to suggestions for LUT improvements for future products. An empirical offset correction had to be applied to the VRS fit factors going into the  $K_d$ -blue product. The TROPOMI  $K_d$ -blue product is therefore not independent from the OLCI wavelength-converted  $K_d(490)$  products used as reference. A correlation with the retrieved atmospheric  $\text{O}_4$  columns was found that might cause this offset. Finding a correction that aims at the origin of this problem and is independent from other  $K_d$  data sets is desirable.

This study presents the first direct satellite retrievals of  $K_d$  in the UV spectral range. We view the TROPOMI  $K_d$  products as potentially gap-filling, providing information in wavelength regions not accessible with current and, to some extent, also planned ocean color sensors and therefore highly encourage further exploration of TROPOMI data for oceanic UV applications. Valuable information can be drawn in more

than 95% of the open ocean. At the current state, TROPOMI  $K_d$  products for scenes with  $K_d < 0.3 \text{ m}^{-1}$  show reasonable uncertainties. In clear water regions, the TROPOMI  $K_d$  products might even outperform the multispectral  $K_d$  products from a theoretical point of view. More extensive comparisons with *in-situ* data is necessary to answer this question. This study therefore also stresses the need for collecting high-quality *in-situ* radiometric measurements in the UV spectral range. As a next step, a  $K_d$  time series over the TROPOMI recording time period can be derived and analyzed on global scales to investigate temporal and spatial stability of the products. Once thoroughly validated, TROPOMI  $K_d$ -UV data sets can be used, e.g., for modeling of photochemical reaction rates of climatically important chemical substances (Smyth, 2011) and for estimating UV dose rates in combination with mixed layer depth data and UV irradiance above surface (Vasilkov et al., 2001; Smyth, 2011). Intercomparison of the three spectral TROPOMI-derived  $K_d$  in the UV-VIS region can give insight on CDOM origin and production of UV-protective pigments by phytoplankton and be used as an indicator for UV-sensitive and optically interesting regions in the open ocean.

## DATA AVAILABILITY STATEMENT

The TROPOMI  $K_d$  data for the three wavelengths regions and the *in-situ* spectrally resolved  $K_d$  data are stored at PANGAEA Bracher and Dinter (2021), Bracher et al. (2022), Oelker et al. (2022). All other data are already publicly available as cited in section 2.

## AUTHOR CONTRIBUTIONS

JO extended the algorithm to the UV domain, performed DOAS retrievals, RTM simulations, designed and carried out the sensitivity analysis, calculated the resulting  $K_d$  product as well as the comparisons with *in-situ* and multispectral data, and wrote the first draft of the manuscript. SL helped with comparisons of TROPOMI-derived  $K_d$  products to multispectral and *in-situ* data sets and their discussion. AR provided the software for the DOAS retrievals and gave advice with respect to retrieval settings and use of cloud products. AB initiated the project, gave the idea for the  $K_d$ -UV retrievals as well as provided the *in-situ*  $K_d$  data set, drafted the revision of the manuscript, and the answers to the reviewers. All authors reviewed the drafts presented by JO and AB, and gave valuable comments on presentation of results and their discussion as well as structure of the manuscript. All authors contributed to the article and approved the submitted version.

## FUNDING

The main funding for this study was provided by the ESA S5P+Innovation Theme 7 Ocean Colour (S5POC) project (No 4000127533/19/I-NS). The contribution by SL was partially funded by the Deutsche Forschungsgemeinschaft (DFG, German Research Foundation)–Project number 268020496–TRR 172,

within the Transregional Collaborative Research Center Arctic Amplification: Climate Relevant Atmospheric and Surface Processes, and Feedback Mechanisms (AC3) (Project C03), and was also partially made in the framework of the state assignment of the Federal Agency for Scientific Organizations (FASO) Russia (theme 0128-2021-0014). Support for the sampling of *in-situ* data was provided by the Helmholtz Infrastructure Initiative FRAM. Ship time was provided under grant AWI\_PS113\_00.

## ACKNOWLEDGMENTS

We would like to thank the European Space Agency for funding this project in the frame of the Sentinel-5P + Innovation projects. Special thanks go to Marie-Helene Rio, project coordinator at ESA, for shaping the project focus on UV irradiation with us and supporting our ideas. We value the fruitful discussions during project meetings beneficial for the outcome of this manuscript. We further thank ESA and the Climate Change Initiative and EUMETSAT for the multispectral  $K_d$  data sets.

## REFERENCES

- Austin, R. W., and Petzold, T. J. (1981). *The Determination of the Diffuse Attenuation Coefficient of Sea Water Using the Coastal Zone Color Scanner*. Boston, MA: Springer US. doi: 10.1007/978-1-4613-3315-9\_29
- Baker, K. S., and Smith, R. C. (1982). Bio-optical classification and model of natural waters. *Limnol. Oceanogr.* 27, 500–509. doi: 10.4319/lo.1982.27.3.0500
- Blum, M., Rozanov, V. V., Burrows, J. P., and Bracher, A. (2012). Coupled ocean-atmosphere radiative transfer model in the framework of software package SCIATRAN: selected comparisons to model and satellite data. *Adv. Space Res.* 49, 1728–1742. doi: 10.1016/j.asr.2012.02.012
- Bracher, A., and Dinter, T. (2021). Mean spectral diffuse attenuation coefficients from 318 to 952 nm of underwater light profiles measured at discrete stations with radiometry during RV Polarstern cruise PS113 in the Atlantic Ocean. *PANGAEA*. doi: 10.1594/PANGAEA.931480
- Bracher, A., Dinter, T., and von Appen, W.-J. (2022). Mean spectral diffuse attenuation coefficients from 320 to 917 nm from high spectrally resolved radiometric underwater light transmission profiles obtained by an undulating platform towed behind the ship. *PANGAEA*. doi: 10.1594/PANGAEA.939927
- Bracher, A., Vountas, M., Dinter, T., Burrows, J. P., Röttgers, R., and Peeken, I. (2009). Quantitative observation of cyanobacteria and diatoms from space using PhytoDOAS on SCIAMACHY data. *Biogeosciences* 6, 751–764. doi: 10.5194/bg-6-751-2009
- Bracher, A., Xi, H., Dinter, T., Mangin, A., Strass, V., von Appen, W.-J., et al. (2020). High resolution water column phytoplankton composition across the Atlantic Ocean from ship-towed vertical undulating radiometry. *Front. Mar. Sci.* 7, 235. doi: 10.3389/fmars.2020.00235
- Bracher, A. U., and Wiencke, C. (2000). Simulation of the effects of naturally enhanced UV radiation on photosynthesis of antarctic phytoplankton. *Mar. Ecol. Prog. Ser.* 196, 127–141. doi: 10.3354/meps196127
- Brewin, R. J., Sathyendranath, S., Muller, D., Brockmann, C., Deschamps, P.-Y., Devred, E., et al. (2015). The ocean colour climate change initiative: III. A round-robin comparison on in-water bio-optical algorithms. *Remote Sens. Environ.* 162, 271–294. doi: 10.1016/j.rse.2013.09.016
- Burrows, J. P., Platt, U., and Borrell, P. (2011). *Tropospheric Remote Sensing from Space*. Berlin; Heidelberg: Springer. doi: 10.1007/978-3-642-14791-3\_1
- Chance, K., and Kurucz, R. L. (2010). An improved high-resolution solar reference spectrum for earth's atmosphere measurements in the ultraviolet, visible, and near infrared. *J. Quant. Spectrosc. Radiat. Transfer* 111, 1289–1295. doi: 10.1016/j.jqsrt.2010.01.036
- We thank H. Xi, AWI, and S. Wiegmann, AWI, for supporting PS113 underwater light measurements and the captain, the crew and other scientists on board PS113 for their valuable support on board. We appreciate the work space and resources at the AWI and the IUP. We thank T. Dinter, AWI, for sharing Sentinel-3 visualization tools. JO was grateful for discussions on general structure and presentation of results with J. Rückert, IUP. We thank V. Rozanov, IUP, for helpful discussions regarding SCIATRAN parametrization and L. Alvarado, AWI, for assisting AB in visualizing TROPOMI detailed fit results and discussion on retrieval uncertainty. This study has evolved from the PhD thesis of Oelker (2021). Thanks to the reviewers and the editor for their valuable comments and suggestions that greatly improved this work.

## SUPPLEMENTARY MATERIAL

The Supplementary Material for this article can be found online at: <https://www.frontiersin.org/articles/10.3389/fmars.2022.787992/full#supplementary-material>

- Conde, D., Aubriot, L., and Sommaruga, R. (2000). Changes in UV penetration associated with marine intrusions and freshwater discharge in a shallow coastal Lagoon of the southern Atlantic Ocean. *Marine Ecology Progress Series* 207, 19–31. doi: 10.3354/meps207019
- Cullen, J. J., and Neale, P. J. (1994). Ultraviolet radiation, ozone depletion, and marine photosynthesis. *Photosynth. Res.* 39, 303–320. doi: 10.1007/BF00014589
- Dinter, T., Rozanov, V. V., Burrows, J. P., and Bracher, A. (2015). Retrieving the availability of light in the ocean utilising spectral signatures of vibrational Raman scattering in hyper-spectral satellite measurements. *Ocean Sci.* 11, 373–389. doi: 10.5194/os-11-373-2015
- EUMETSAT (2021). *Recommendations for Sentinel-3 OLCI Ocean Colour Product Validations in Comparison with In Situ Measurements-Matchup Protocols*. Technical report, EUMETSAT.
- Fichot, C. G., Sathyendranath, S., and Miller, W. L. (2008). SeaUV and seaUVc: algorithms for the retrieval of UV/visible diffuse attenuation coefficients from ocean color. *Remote Sens. Environ.* 112, 1584–1602. doi: 10.1016/j.rse.2007.08.009
- Frouin, R., and Iacobellis, S. F. (2002). Influence of phytoplankton on the global radiation budget. *J. Geophys. Res. Atmos.* 107, ACL 5-1?ACL 5-10. doi: 10.1029/2001JD000562
- Frouin, R., Ramon, D., Boss, E., Jolivet, D., Compiègne, M., Tan, J., et al. (2018). Satellite radiation products for ocean biology and biogeochemistry: needs, state-of-the-art, gaps, development priorities, and opportunities. *Front. Mar. Sci.* 5, 3. doi: 10.3389/fmars.2018.00003
- Frouin, R. J., Franz, B. A., Ibrahim, A., Knobelspiesse, K., Ahmad, Z., Cairns, B., et al. (2019). Atmospheric correction of satellite ocean-color imagery during the pace era. *Front. Earth Sci.* 7, 145. doi: 10.3389/feart.2019.00145
- Gomes, A., Bernardo, N., Carmo, A., Rodrigues, T., and Alcantara, E. (2018). Diffuse attenuation coefficient retrieval in cdom dominated inland water with high chlorophyll-a concentrations. *Remote Sens.* 10, 1063. doi: 10.3390/rs10071063
- Grainger, J. F., and Ring, J. (1962). Anomalous Fraunhofer line profiles. *Nature* 193, 762. doi: 10.1038/193762a0
- Haltrin, V. I., and Kattawar, G. W. (1993). Self-consistent solutions to the equation of transfer with elastic and inelastic scattering in oceanic optics: I. *Model. Appl. Opt.* 32, 5356–5367. doi: 10.1364/AO.32.005356
- Højerslev, N., and Aas, E. (1991). A relationship for the penetration of ultraviolet B radiation into the Norwegian sea. *J. Geophys. Res. Oceans* 96, 17003–17005. doi: 10.1029/91JC01822
- IOCCG (2008). *Why Ocean Colour? The Societal Benefits of Ocean-Colour Technology*. Reports of the International Ocean Colour Coordinating Group. IOCCG, Dartmouth, NS.

- Irie, H., Nakayama, T., Shimizu, A., Yamazaki, A., Nagai, T., Uchiyama, A., et al. (2015). Evaluation of max-DOAS aerosol retrievals by coincident observations using crds, lidar, and sky radiometer Intsukuba, Japan. *Atmos. Meas. Tech.* 8, 2775–2788. doi: 10.5194/amt-8-2775-2015
- Jamet, C., Loisel, H., and Dessailly, D. (2012). Retrieval of the spectral diffuse attenuation coefficient  $k_d(\lambda)$  in open and coastal ocean waters using a neural network inversion. *J. Geophys. Res. Oceans* 117, C10. doi: 10.1029/2012JC008076
- Johannessen, S. C., Miller, W. L., and Cullen, J. J. (2003). Calculation of UV attenuation and colored dissolved organic matter absorption spectra from measurements of ocean color. *J. Geophys. Res. Oceans* 108, C9. doi: 10.1029/2000JC000514
- Kara, A. B., Hurlburt, H. E., Rochford, P. A., and O'Brien, J. J. (2004). The impact of water turbidity on interannual sea surface temperature simulations in a layered global ocean model. *J. Phys. Oceanogr.* 34, 345–359. doi: 10.1175/1520-0485(2004)034<0345:TIOWTO>2.0.CO;2
- Lee, Z., Carder, K. L., and Arnone, R. A. (2002). Deriving inherent optical properties from water color: a multiband quasi-analytical algorithm for optically deep waters. *Appl. Opt.* 41, 5755–5772. doi: 10.1364/AO.41.005755
- Lee, Z., Hu, C., Shang, S., Du, K., Lewis, M., Arnone, R., et al. (2013). Penetration of UV-visible solar radiation in the global oceans: insights from ocean color remote sensing. *J. Geophys. Res. Oceans* 118, 4241–4255. doi: 10.1002/jgrc.20308
- Lee, Z.-P., Darecki, M., Carder, K. L., Davis, C. O., Stramski, D., and Rhea, W. J. (2005a). Diffuse attenuation coefficient of downwelling irradiance: an evaluation of remote sensing methods. *J. Geophys. Res. Oceans* 110, C02017. doi: 10.1029/2004JC002573
- Lee, Z.-P., Du, K.-P., and Arnone, R. (2005b). A model for the diffuse attenuation coefficient of downwelling irradiance. *J. Geophys. Res. Oceans* 110, C02016. doi: 10.1029/2004JC002275
- Lewis, M. R., Carr, M.-E., Feldman, G. C., Esaias, W., and McClain, C. (1990). Influence of penetrating solar radiation on the heat budget of the equatorial Pacific Ocean. *Nature* 347, 543–545. doi: 10.1038/347543a0
- Longhurst, A., Sathyendranath, S., Platt, T., and Caverhill, C. (1995). An estimate of global primary production in the ocean from satellite radiometer data. *J. Plankton Res.* 17, 1245–1271. doi: 10.1093/plankt/17.6.1245
- Ludewig, A., Kleipool, Q., Bartstra, R., Landzaat, R., Leloux, J., Loots, E., et al. (2020). In-flight calibration results of the TROPOMI payload on board the Sentinel-5 Precursor satellite. *Atmos. Meas. Tech.* 13, 3561–3580. doi: 10.5194/amt-13-3561-2020
- Mason, J. D., Cone, M. T., and Fry, E. S. (2016). Ultraviolet (250–550 nm) absorption spectrum of pure water. *Appl. Opt.* 55, 7163–7172. doi: 10.1364/AO.55.007163
- Miller, A. J., Alexander, M. A., Boer, G. J., Chai, F., Denman, K., Erickson, D., J., et al. (2003). Potential feedbacks between Pacific Ocean ecosystems and interdecadal climate variations. *Bull. Am. Meteorol. Soc.* 84, 617–634. doi: 10.1175/BAMS-84-5-617
- Mobley, C., and Sundman, L. (2013). *HydroLight 5.2 - EcoLight 5.2 Technical Documentation*. Technical report, Sequoia Scientific, Inc.
- Morel, A., and Antoine, D. (1994). Heating rate within the upper ocean in relation to its bio-optical state. *J. Phys. Oceanogr.* 24, 1652–1665. doi: 10.1175/1520-0485(1994)024<1652:HRWTUO>2.0.CO;2
- Morel, A., Claustre, H., Antoine, D., and Gentili, B. (2007a). Natural variability of bio-optical properties in case 1 waters: attenuation and reflectance within the visible and near-UV spectral domains, as observed in south pacific and mediterranean waters. *Biogeosciences* 4, 913–925. doi: 10.5194/bg-4-913-2007
- Morel, A., Huot, Y., Gentili, B., Werdell, P. J., Hooker, S. B., and Franz, B. A. (2007b). Examining the consistency of products derived from various ocean color sensors in open ocean (case 1) waters in the perspective of a multi-sensor approach. *Remote Sens. Environ.* 111, 69–88. doi: 10.1016/j.rse.2007.03.012
- Morel, A., and Maritorena, S. (2001). Bio-optical properties of oceanic waters: a reappraisal. *J. Geophys. Res. Oceans* 106, 7163–7180. doi: 10.1029/2000JC000319
- Nelson, N. B., and Siegel, D. A. (2002). “Chapter 11: Chromophoric DOM in the open ocean,” in *Biogeochemistry of Marine Dissolved Organic Matter*, eds D. A. Hansell and C. A. Carlson (San Diego, CA: Academic Press), 547–578. doi: 10.1016/B978-012323841-2/50013-0
- Nicolaus, M., Hudson, S. R., Gerland, S., and Munderloh, K. (2010). A modern concept for autonomous and continuous measurements of spectral Albedo and transmittance of sea ice. *Cold Regions Sci. Technol.* 62, 14–28. doi: 10.1016/j.coldregions.2010.03.001
- Oelker, J. (2021). *Suitability of atmospheric satellite sensors for ocean color applications* (PhD thesis). Department of Physics and Engineering, University Bremen, Bremen, Germany.
- Oelker, J., Richter, A., Dinter, T., Rozanov, V. V., Burrows, J. P., and Bracher, A. (2019). Global diffuse attenuation derived from vibrational raman scattering detected in hyperspectral backscattered satellite spectra. *Opt. Express* 27, A829–A855. doi: 10.1364/OE.27.00A829
- Oelker, J., Richter, A., Losa, S. N., Alvarado, L. M. A., Bracher, A. (2022). Mean spectral diffuse attenuation coefficients averaged for 320 nm to 338.5 nm (UVAB), 356.5 nm to 390 nm (UVA) and 390 nm to 423 nm (blue) in the Atlantic Ocean from Sentinel-5P instrument TROPOMI. PANGAEA. doi: 10.1594/PANGAEA.940352
- Ohlmann, J. C., Siegel, D. A., and Gautier, C. (1996). Ocean mixed layer radiant heating and solar penetration: a global analysis. *J. Clim.* 9, 2265–2280. doi: 10.1175/1520-0442(1996)009<2265:OMLRHA>2.0.CO;2
- Okamura, Y., Yamada, Y., Urabe, T., Ando, S., and Tanaka, K. (2019). “In-orbit observation of the Second Generation Global Imager (SGLI) and study towards follow-on imaging radiometer,” in *IGARSS 2019 - 2019 IEEE International Geoscience and Remote Sensing Symposium* (Yokohama), 5792–5795. doi: 10.1109/IGARSS.2019.8900124
- Perner, D., and Platt, U. (1979). Detection of nitrous acid in the atmosphere by differential optical absorption. *Geophys. Res. Lett.* 6, 917–920. doi: 10.1029/GL006i012p00917
- Peters, E., Wittrock, F., Richter, A., Alvarado, L. M. A., Rozanov, V. V., and Burrows, J. P. (2014). Liquid water absorption and scattering effects in DOAS retrievals over oceans. *Atmos. Meas. Tech.* 7, 4203–4221. doi: 10.5194/amt-7-4203-2014
- Platt, T. (1986). Primary production of the ocean water column as a function of surface light intensity: algorithms for remote sensing. *Deep Sea Res. A Oceanogr. Res. Pap.* 33, 149–163. doi: 10.1016/0198-0149(86)90115-9
- Platt, U., and Stutz, J. (2008). *Differential Optical Absorption Spectroscopy*. Berlin; Heidelberg: Springer.
- Pope, R. M., and Fry, E. S. (1997). Absorption spectrum (380–700 nm) of pure water. II. Integrating cavity measurements. *Appl. Opt.* 36, 8710–8723. doi: 10.1364/AO.36.008710
- Prieur, L., and Sathyendranath, S. (1981). An optical classification of coastal and oceanic waters based on the specific spectral absorption curves of phytoplankton pigments, dissolved organic matter, and other particulate materials. *Limnol. Oceanogr.* 26, 671–689. doi: 10.4319/lo.1981.26.4.0671
- Remer, L. A., Kleidman, R. G., Levy, R. C., Kaufman, Y. J., Tanré, D., Mattoo, S., et al. (2008). Global aerosol climatology from the MODIS satellite sensors. *J. Geophys. Res. Atmos.* 113, D14SD07. doi: 10.1029/2007JD009661
- Richter, A. (1997). *Measurements of stratospheric trace species above Bremen, 53N using absorption spectroscopy* (dissertation). University of Bremen, Bremen, Germany.
- Richter, A. (2009). *Algorithm Theoretical Basis Document for the GOME-2 Rapid Volcanic SO<sub>2</sub> Product*. Technical report, Insitute of Environmental Physics, University of Bremen.
- Rothman, L. S., Gordon, I. E., Babikov, Y., Barbe, A., Benner, D. C., Bernath, P. F., et al. (2013). The HITRAN2012 molecular spectroscopic database. *J. Quant. Spectrosc. Radiat. Transfer* 130, 4–50. doi: 10.1016/j.jqsrt.2013.07.002
- Rozanov, V. V., Dinter, T., Rozanov, A. V., Wolanin, A., Bracher, A., and Burrows, J. P. (2017). Radiative transfer modeling through terrestrial atmosphere and ocean accounting for inelastic processes: Software package SCIATRAN. *J. Quant. Spectrosc. Radiat. Transfer* 194, 65–85. doi: 10.1016/j.jqsrt.2017.03.009
- Rozanov, V. V., Rozanov, A. V., Kokhanovsky, A. A., and Burrows, J. P. (2014). Radiative transfer through terrestrial atmosphere and ocean: software package SCIATRAN. *J. Quant. Spectrosc. Radiat. Transfer* 133, 13–71. doi: 10.1016/j.jqsrt.2013.07.004
- Sadeghi, A., Dinter, T., Vountas, M., Taylor, B. B., Altenburg-Soppa, M., Peeken, I., et al. (2012). Improvement to the PhytoDOAS method for identification of coccolithophores using hyper-spectral satellite data. *Ocean Sci.* 8, 1055–1070. doi: 10.5194/os-8-1055-2012

- Sathyendranath, S., Brewin, R., Brockmann, C., Brotas, V., Calton, B., Chuprin, A., et al. (2019). An ocean-colour time series for use in climate studies: the experience of the ocean-colour climate change initiative (OC-CCI). *Sensors* 19, 4285. doi: 10.3390/s19194285
- Sathyendranath, S., GoUveia, A. D., Shetye, S. R., Ravindran, P., and Platt, T. (1991). Biological control of surface temperature in the arabian sea. *Nature* 349, 54–56. doi: 10.1038/349054a0
- Sathyendranath, S., Jackson, T., Brockmann, C., Brotas, V., Calton, B., Chuprin, A., et al. (2020). *ESA Ocean Colour Climate Change Initiative (ocean\_colour\_cci): Global Chlorophyll-A Data Products Gridded on a Sinusoidal Projection, Version 4.2*. Centre for Environmental Data Analysis. Technical report.
- Sathyendranath, S., Platt, T., Caverhill, C. M., Warnock, R. E., and Lewis, M. R. (1989). Remote sensing of oceanic primary production: computations using a spectral model. *Deep Sea Res. A. Oceanogr. Res. Pap.* 36, 431–453. doi: 10.1016/0198-0149(89)90046-0
- Seegers, B. N., Stumpf, R. P., Schaeffer, B. A., Loftin, K. A., and Werdell, P. J. (2018). Performance metrics for the assessment of satellite data products: an ocean color case study. *Opt. Express* 26, 7404–7422. doi: 10.1364/OE.26.007404
- Seo, S., Richter, A., Blechschmidt, A.-M., Bougoudis, I., and Burrows, J. P. (2019). First high-resolution bro column retrievals from tropomi. *Atmos. Meas. Tech.* 12, 2913–2932. doi: 10.5194/amt-12-2913-2019
- Serdychenko, A., Gorshchev, V., Weber, M., Chehade, W., and Burrows, J. P. (2014). High spectral resolution ozone absorption cross-sections-Part 2: temperature dependence. *Atmos. Meas. Tech.* 7, 625–636. doi: 10.5194/amt-7-625-2014
- Shell, K. M., Frouin, R., Nakamoto, S., and Somerville, R. C. J. (2003). Atmospheric response to solar radiation absorbed by phytoplankton. *J. Geophys. Res. Atmos.* 108, D15. doi: 10.1029/2003JD003440
- Shen, M., Duan, H., Cao, Z., Xue, K., Loiselle, S., and Yesou, H. (2017). Determination of the downwelling diffuse attenuation coefficient of lake water with the sentinel-3a OLCI. *Remote Sens.* 9, 1246. doi: 10.3390/rs9121246
- Siegel, D. A., Maritorena, S., Nelson, N. B., Hansell, D. A., and Lorenzi-Kayser, M. (2002). Global distribution and dynamics of colored dissolved and detrital organic materials. *J. Geophys. Res. Oceans* 107, 21-1–21-14. doi: 10.1029/2001JC000965
- Sinha, R. P., and Hader, D.-P. (2002). UV-induced dna damage and repair: a review. *Photochem. Photobiol. Sci.* 1, 225–236. doi: 10.1039/b201230h
- Smyth, T. J. (2011). Penetration of UV irradiance into the global ocean. *J. Geophys. Res. Oceans* 116, C11. doi: 10.1029/2011JC007183
- Spinei, E., Cede, A., Herman, J., Mount, G. H., Eloranta, E., Morley, B., et al. (2015). Ground-based direct-sun doas and airborne max-DOAS measurements of the collision-induced oxygen complex,  $\text{o}_2\text{o}_2$ , absorption with significant pressure and temperature differences. *Atmos. Meas. Tech.* 8, 793–809. doi: 10.5194/amt-8-793-2015
- Tanskanen, A., Maatta, A., Krotkov, N., Herman, J., Kaurola, J., Koskela, T., et al. (2006). Surface ultraviolet irradiance from omi. *IEEE Trans. Geosci. Remote Sens.* 44, 1267–1271. doi: 10.1109/TGRS.2005.862203
- Thalman, R., and Volkamer, R. (2013). Temperature dependent absorption cross-sections of O<sub>2</sub>-O<sub>2</sub> collision pairs between 340 and 630 nm and at atmospherically relevant pressure. *Phys. Chem. Chem. Phys.* 15, 15371–15381. doi: 10.1039/c3cp50968k
- Tilstone, G., Dall'2019Olmo, G., Hieronymi, M., Ruddick, K., Beck, M., Ligi, M., et al. (2020). Field intercomparison of radiometer measurements for ocean colour validation. *Remote Sens.* 12, 10. doi: 10.3390/rs12101587
- van der Does, M., Korte, L. F., Munday, C. I., Brummer, G.-J. A., and Stuut, J.-B. W. (2016). Particle size traces modern Saharan dust transport and deposition across the equatorial North Atlantic. *Atmos. Chem. Phys.* 16, 13697–13710. doi: 10.5194/acp-16-13697-2016
- van Geffen, J., Boersma, K. F., Eskes, H., Sneep, M., ter Linden, M., Zara, M., et al. (2020). S5p TROPOMI  $\text{no}_2$  slant column retrieval: method, stability, uncertainties and comparisons with OMI. *Atmos. Meas. Tech.* 13, 1315–1335. doi: 10.5194/amt-13-1315-2020
- van Geffen, J., Eskes, H., Boersma, K., Maasakkers, J., and Veefkind, J. (2019). *TROPOMI ATBD of the total and tropospheric NO<sub>2</sub> data products*. Technical report, Royal Netherlands Meteorological Institute.
- Vandaele, A., Hermans, C., Simon, P., Carleer, M., Colin, R., Fally, S., et al. (1998). Measurements of the  $\text{no}_2$  absorption cross-section from 42 000  $\text{cm}^{-1}$  to 10 000  $\text{cm}^{-1}$  (238–1000 nm) at 220 k and 294 k. *J. Quant. Spectrosc. Radiat. Transfer* 59, 171–184. doi: 10.1016/S0022-4073(97)00168-4
- Vasilkov, A., Krotkov, N., Herman, J., McClain, C., Arrigo, K., and Robinson, W. (2001). Global mapping of underwater UV irradiances and dna-weighted exposures using total ozone mapping spectrometer and sea-viewing wide field-of-view sensor data products. *J. Geophys. Res.* 106, 27205–27219. doi: 10.1029/2000JC000373
- Vasilkov, A. P., Herman, J. R., Ahmad, Z., Kahru, M., and Mitchell, B. G. (2005). Assessment of the ultraviolet radiation field in ocean waters from space-based measurements and full radiative-transfer calculations. *Appl. Opt.* 44, 2863–2869. doi: 10.1364/AO.44.002863
- Vasilkov, A. P., Herman, J. R., Krotkov, N. A., Kahru, M., Mitchell, B. G., and Hsu, C. (2002a). Problems in assessment of the ultraviolet penetration into natural waters from space-based measurements. *Opt. Eng.* 41, 3019–3027. doi: 10.1117/1.1516822
- Vasilkov, A. P., Joiner, J., Gleason, J., and Bhartia, P. K. (2002b). Ocean Raman scattering in satellite backscatter UV measurements. *Geophys. Res. Lett.* 29, 14–18. doi: 10.1029/2002GL014955
- Veefkind, J., Aben, I., McMullan, K., Förster, H., de Vries, J., Otter, G., et al. (2012). Tropomi on the esa sentinel-5 precursor: a GMEs mission for global observations of the atmospheric composition for climate, air quality and ozone layer applications. *Remote Sens. Environ.* 120, 70–83. doi: 10.1016/j.rse.2011.09.027
- Vernet, M., Brody, E. A., Holm-Hansen, O., and Mitchell, B. G. (1994). The response of Antarctic phytoplankton to ultraviolet radiation: absorption, photosynthesis, and taxonomic composition. *Antarctic Res. Ser.* 62, 143–158. doi: 10.1029/AR062p0143
- Vodacek, A., and Blough, N. V. (1997). “Seasonal variation of CDOM in the Middle Atlantic Bight: terrestrial inputs and photooxidation,” in *Ocean Optics XIII*, eds S. G. Ackleson and R. J. Frouin (Halifax, Nova Scotia: International Society for Optics and Photonics, SPIE), 132–137. doi: 10.4319/lo.1997.42.4.0674
- von Appen, W.-J., Strass, V. H., Bracher, A., Xi, H., Hörstmann, C., Iversen, M. H., et al. (2020). High-resolution physical-biogeochemical structure of a filament and an eddy of upwelled water off northwest africa. *Ocean Sci.* 16, 253–270. doi: 10.5194/os-16-253-2020
- Vonk, F. (2018). *Input/Output Data Specification for the TROPOMI L01b Data Processor*. Technical report, Royal Netherlands Meteorological Institute.
- Vountas, M., Dinter, T., Bracher, A., Burrows, J. P., and Sierk, B. (2007). Spectral studies of ocean water with space-borne sensor SCIAMACHY using Differential Optical Absorption Spectroscopy (DOAS). *Ocean Sci.* 3, 429–440. doi: 10.5194/os-3-429-2007
- Vountas, M., Richter, A., Wittrock, F., and Burrows, J. P. (2003). Inelastic scattering in ocean water and its impact on trace gas retrievals from satellite data. *Atmos. Chem. Phys.* 3, 1365–1375. doi: 10.5194/acp-3-1365-2003
- Vountas, M., Rozanov, V., and Burrows, J. (1998). Ring effect: impact of rotational raman scattering on radiative transfer in earth's atmosphere. *J. Quant. Spectrosc. Radiat. Transfer* 60, 943–961. doi: 10.1016/S0022-4073(97)00186-6
- Walrafen, G. E. (1966). Raman spectral studies of the effects of temperature on water and electrolyte solutions. *J. Chem. Phys.* 44, 1546–1558. doi: 10.1063/1.1726891
- Wang, M., Son, S., and Harding, L. W. Jr. (2009). Retrieval of diffuse attenuation coefficient in the chesapeake bay and turbid ocean regions for satellite ocean color applications. *J. Geophys. Res. Oceans* 114, C10. doi: 10.1029/2009JC005286
- Wang, Y., Lee, Z., Wei, J., Shang, S., Wang, M., and Lai, W. (2021). Extending satellite ocean color remote sensing to the near-blue ultraviolet bands. *Remote Sens. Environ.* 253, 112228. doi: 10.1016/j.rse.2020.112228
- Wittrock, F., Richter, A., Oetjen, H., Burrows, J. P., Kanakidou, M., Myriokefalitakis, S., et al. (2006). Simultaneous global observations of glyoxal and formaldehyde from space. *Geophys. Res. Lett.* 33, L16804. doi: 10.1029/2006GL026310
- Wolanin, A., Rozanov, V. V., Dinter, T., Noël, S., Vountas, M., Burrows, J. P., et al. (2015). Global retrieval of marine and terrestrial chlorophyll

- fluorescence at its red peak using hyperspectral top of atmosphere radiance measurements: feasibility study and first results. *Remote Sens. Environ.* 166, 243–261. doi: 10.1016/j.rse.2015.05.018
- Zepp, R. G., Callaghan, T. V., and Erickson, I. I. I., D. J. (2003). Interactive effects of ozone depletion and climate change on biogeochemical cycles. *Photochem. Photobiol. Sci.* 2, 51–61. doi: 10.1039/b211154n
- Zepp, R. G., Erickson, D. J. III, Paul, N. D., and Sulzberger, B. (2007). Interactive effects of solar UV radiation and climate change on biogeochemical cycling. *Photochem. Photobiol. Sci.* 6, 286–300. doi: 10.1039/b700021a

**Conflict of Interest:** The authors declare that the research was conducted in the absence of any commercial or financial relationships that could be construed as a potential conflict of interest.

**Publisher's Note:** All claims expressed in this article are solely those of the authors and do not necessarily represent those of their affiliated organizations, or those of the publisher, the editors and the reviewers. Any product that may be evaluated in this article, or claim that may be made by its manufacturer, is not guaranteed or endorsed by the publisher.

Copyright © 2022 Oelker, Losa, Richter and Bracher. This is an open-access article distributed under the terms of the Creative Commons Attribution License (CC BY). The use, distribution or reproduction in other forums is permitted, provided the original author(s) and the copyright owner(s) are credited and that the original publication in this journal is cited, in accordance with accepted academic practice. No use, distribution or reproduction is permitted which does not comply with these terms.